The electrochemical reduction of dioxygen and hydrogen peroxide by molecular copper catalysts

Langerman, M.

Appendix A

Supplementary Information for Chapter 2

A.1   Scan rate dependence

The peak redox current was found to be linearly dependent on the square root of the scan rate (Figure A.1) and the peak-to-peak separation ΔEp remained constant at 56 mV ± 5 mV at different scan rates. This is in agreement with a homogeneous system undergoing a reversible one-electron reduction and oxidation step. The diffusion coefficient of Cu-tmpa is $4.9×10{-6}$ cm2 s−1, as derived by the Randles-Sevcik equation.
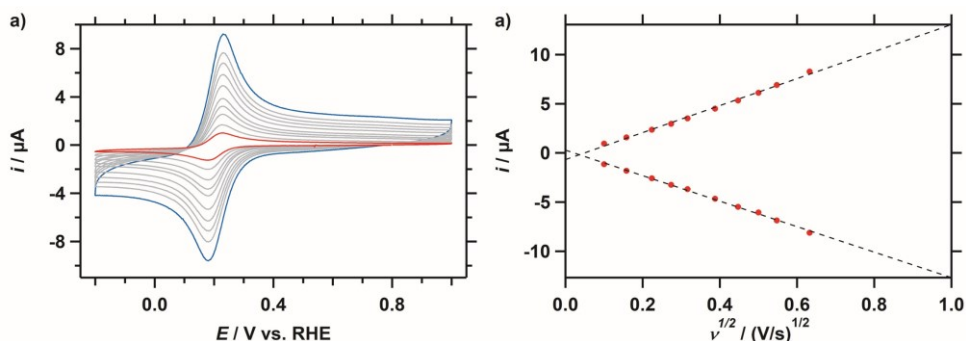

Figure A.1. a) CVs of 0.3 mM Cu-tmpa at a range of scan rates between 400 and 10 mV s^{-1} in the presence of 1 atm Ar. **b)** Plot of the peak oxidative and reductive currents of the redox couple as a function of v$^{1/2}$.

A.2   EQCM measurements

As copper ions have very fast ligand exchange kinetics it is important to establish the homogeneity of the catalyst during the catalytic reaction.[1-2] Therefore, electrochemical quartz crystal microbalance experiments (EQCM) measurements were performed to investigate the stability of Cu-tmpa both under catalytic and non-catalytic conditions. During EQCM measurements, the frequency changes of an oscillating gold-coated quartz crystal are measured during the electrochemical experiment. These frequency changes can be directly correlated to the mass change of the electrode. A decrease in frequency corresponds to an increase in the mass of the electrode, while an increase in frequency corresponds to a decrease in mass. The EQCM experiments
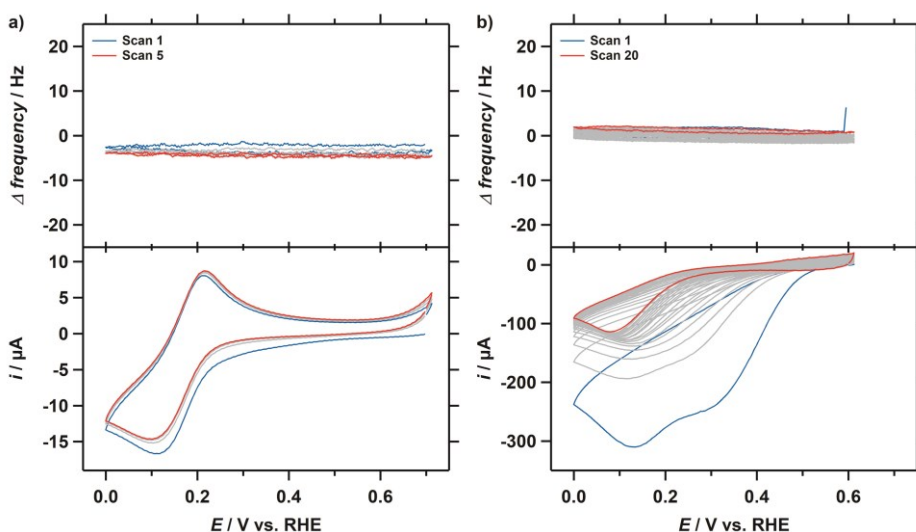
Figure A.2. EQCM experiments in a pH 7 PB (0.1 M), containing 0.3 mM Cu-tmpa. CVs (bottom panel) and the corresponding frequency response (top panel) are shown for both **(a)** argon-saturated and **(b)** oxygen-saturated solutions. CVs were obtained at a scan rate of 100 mV s^{-1}.

were conducted using an Autolab PGSTAT 128N potentiostat and a 5 mL Autolab EQCM cell. An Autolab gold coated quartz crystal EQCM electrode (A = 0.35 cm^2, gold layer thickness = 100 nm) was used as the working electrode and a coiled gold wire was used as the counter electrode. An RHE Luggin setup was used as the reference electrode. Cyclic voltammetry (CV) measurements were performed in a pH 7 phosphate buffer (0.1 M), containing 0.3 mM Cu-tmpa. EQCM measurements in an argon-saturated solution show a well-defined redox couple at 0.20 V, while little change in the frequency of the electrode is observed (Figure A.2a). The EQCM data for Cu-tmpa in a 1 atm O$_2$-saturated solution is shown in Figure A.2b. Over subsequent scans the catalytic current decreases significantly, while at the same time no change in frequency of the electrode is observed during the ORR. The frequency changes observed in the presence of Cu-tmpa are in the same window as the EQCM data obtained for a bare gold electrode in a solution without any Cu-tmpa present (Figure A.3). The decreasing catalytic current corresponds to the depletion of dioxygen in the solution, and this behaviour can also be observed in the EQCM data for the bare gold electrode. These results clearly show that Cu-tmpa forms no surface deposits during the ORR. Comparison to Cu(OTf)$_2$ as a positive control for surface deposition shows clear frequency changes, corresponding to deposition in the presence of Ar followed by surface stripping in the presence of O$_2$, respectively (Figure A.4).
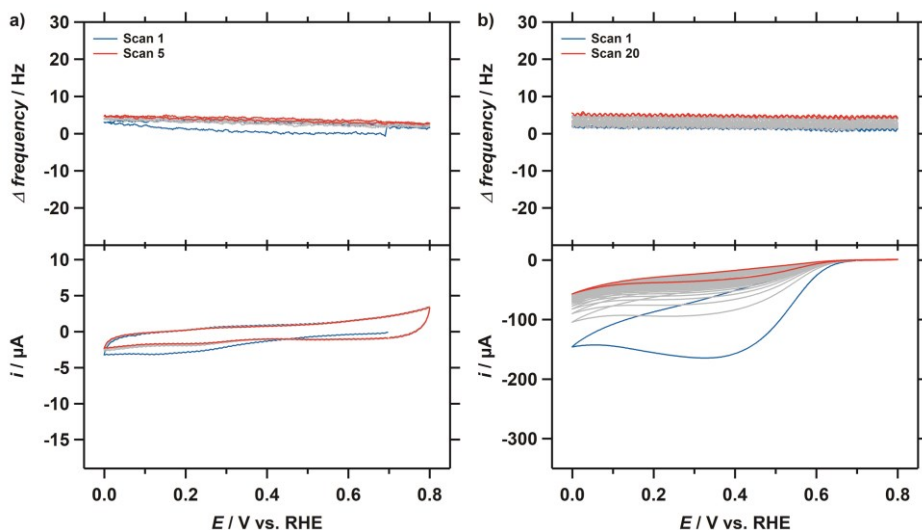
Figure A.3. EQCM experiments in a pH 7 PB (0.1 M). CVs (bottom panel) and the corresponding frequency response (top panel) for the bare gold-coated electrode are shown for both **(a)** argon-saturated and **(b)** oxygen-saturated solutions. CVs were measured at a scan rate of 100 mV s^{-1}.
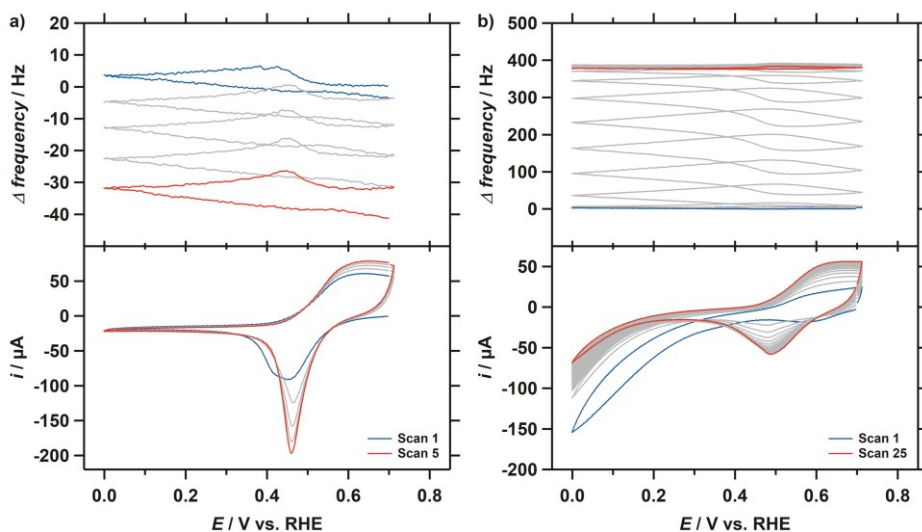

Figure A.4. EQCM experiments in a pH 7 PB (0.1 M), containing 0.3 mM Cu(OTf)$_2$. CVs (bottom panel) and the corresponding frequency response (top panel) are shown for both **(a)** argon-saturated and **(b)** oxygen-saturated solutions. CVs were measured at a scan rate of 100 mV s^{-1}.

A.3   Concentration dependence studies

For the determination of the catalytic current i_{cat} at low Cu-tmpa concentrations, the GC electrode was polished with 0.05 µm alumina suspension for 5 minutes and subsequently sonicated in MilliQ for 15 minutes before every measurement. Additionally, a blank CV was measured of the GC electrode in an oxygen-saturated pH 7 PB electrolyte solution after every electrode polish. The currents obtained from CV measurements in presence of Cu-tmpa were corrected using their corresponding blank measurement, giving the catalytic current without any contribution from the GC electrode.
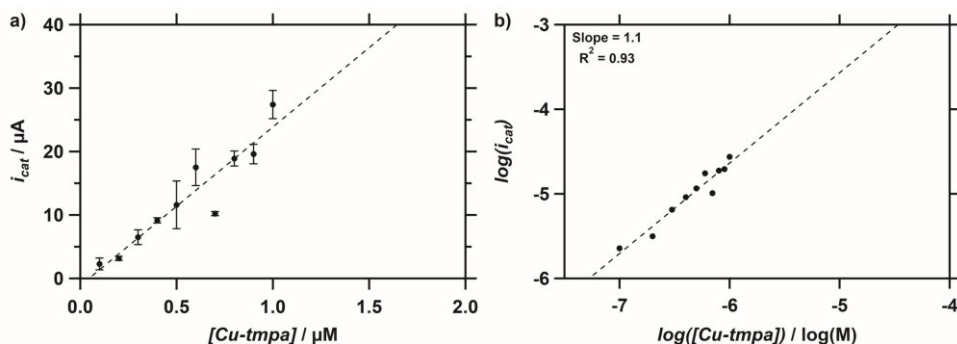

Figure A.5. a) Background corrected catalytic current i_{cat} as a function of Cu-tmpa concentration. **b)** Log-log plot of the same data.

A.4   RRDE experiments

RRDE experiments were conducted using an Autolab PGSTAT 12 potentiostat and a Pine Instruments MSR rotator. All measurements were done in a custom-build glass two-compartment cell with a three-electrode setup. A gold wire was used as a counter electrode, separated from the main compartment by a glass frit. GC disks (A = 0.196 cm^2) and Pt disks (A = 0.196 cm^2) were used in conjunction with a Pt ring in a Pine Instruments E6R1 ChangeDisk setup. Prior to use, the electrodes were separately manually polished for 5 minutes with 1.0, 0.3, and 0.05 µm alumina suspensions on Buehler cloth polishing pads, for 5 minutes respectively, followed by sonication in Milli-Q water for 15 minutes. Additionally, the Pt disk was electropolished by CV between -0.5 V and 2 V vs. RHE at 1 V/s for 200 cycles in an aqueous 0.1 M H$_2$SO$_4$ solution. The collection efficiency (N = 0.23) of the Pt ring electrode was determined from the one-electron transfer Cu$^{II/I}$ redox reaction of Cu-tmpa, which is slightly lower than the collection efficiency supplied by the manufacturer (N = 0.25, Pine Instruments). This is in good agreement with the collection efficiency (22%) previously obtained for the [Fe(CN)$_6$]$^{4-}$/Fe(CN)$_6$]$^{3-}$ redox couple using the same setup.[3] The current measured in

the absence of Cu-tmpa were subtracted from I_{ring} and I_{disk} obtained in the presence of Cu-tmpa and the resulting background corrected LSVs are shown in Figure A.5.
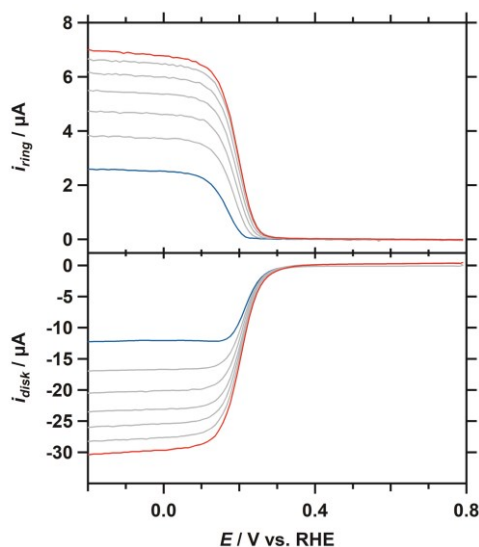

Figure A.6. RRDE LSV data used to determine the collection efficiency of the Pt ring electrode, 400 to 2800 RPM, 400 RPM increments. Conditions: pH 7 phosphate buffer ([PO₄] = 100 mM), [Cu-tmpa] = 0.3 mM, 293 K, 50 mV s⁻¹ scan rate.

A.5   Koutecky-Levich analysis

The limiting currents at different rotation rates for the ORR by Cu-tmpa shown in Figure 2.4 (main text) show good linearity in accordance with the behaviour described by the Koutecky-Levich equation:

$$\frac{1}{I} = \frac{1}{I_K} + \frac{1}{I_L} \tag{A.1}$$

Where I_K is the kinetic current and I_L is the mass-transport limited current. I_L can be described through the Levich equation:

$$I_L = 0.62nFAD^{2/3}v^{-1/6}C\omega^{1/2} = B\omega^{1/2} \tag{A.2}$$

Where n is the electron transfer number, F is the faradaic constant (C/mol), A is the surface area of the disk electrode (cm²), D is the diffusion coefficient of O_2 (cm²/s), v is the kinematic viscosity (cm²/s), C is the concentration of O_2 (mol/cm³), and ω the rotation rate (rad/s). These constants can be simplified with the Levich constant B. The linear relationship observed in the Koutecky-Levich plot provides a B value for the 4-electron ORR, according to Eq. A.3.
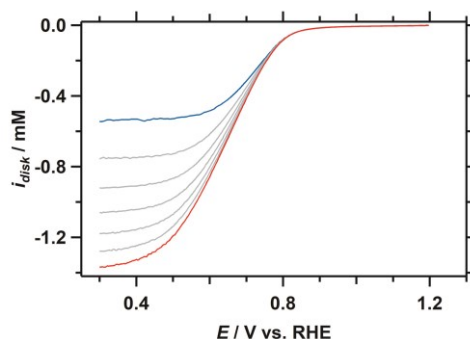
$$slope = \frac{1}{B} \tag{A.3}$$

Figure A.7. RDE LSVs of polycrystalline Pt disk under 1 atm O$_2$ at different rotation rates from 400 RPM (blue line) to 2800 RPM (red line), 400 RPM increments. Conditions: pH 7 phosphate buffer ([PO$_4$] = 100 mM), 293 K, 50 mV s^{-1} scan rate.

A Pt disk was used to obtain a reference *B* value for the 4-electron ORR under our experimental conditions This was done by measuring the ORR activity of a Pt disk at different rotation rates under the exact same conditions as the Cu-tmpa system, as shown in Figure A.7. Some discussion has arisen around the viability of the KL analysis for the ORR reaction.[4] Indeed, we also note that the *n* determined by the KL method (n_{KL}) is not entirely independent of the angular velocity ω. However, determination of *n* by the RRDE method (n_{RRDE}) show similar values of *n* in the mass-transport limited regime.
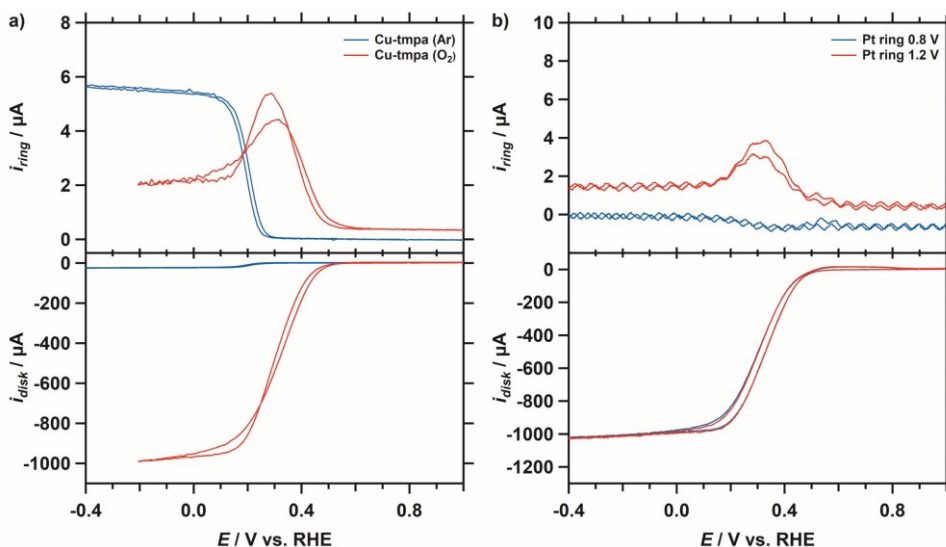

Figure A.8. a) RRDE CV comparison of Cu-tmpa under 1 atm Ar (blue line) or 1 atm O$_2$ (red line) at 1600 RPM. **b)** RRDE CV comparison of Cu-tmpa with the Pt ring potential set at 1.2 V (red line) or 0.8 V (blue line) vs. RHE under 1 atm O$_2$ at 1600 RPM. Conditions: pH 7 phosphate buffer ([PO$_4$] = 100 mM), [Cu-tmpa] = 0.3 mM, 293 K, 50 mV s^{-1} scan rate.
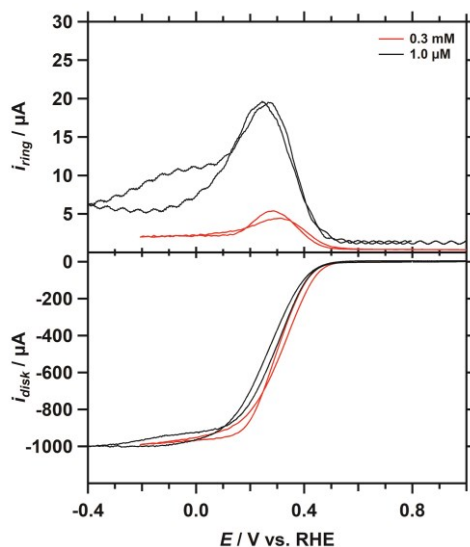
Figure A.9. RRDE CV comparison of the ORR at different Cu-tmpa concentrations. Conditions: pH 7 phosphate buffer ([PO$_4$] = 100 mM), 293 K, Pt ring at 1.2 V vs. RHE, 50 mV s^{-1} scan rate.

A.6   Collection efficiency of H$_2$O$_2$ at the Pt ring

For the quantification of H$_2$O$_2$ at the Pt ring the collection efficiency towards H$_2$O$_2$ was determined. As the catalytic conversion of H$_2$O$_2$ to O$_2$ by Pt involves a reversible surface binding step, the collection efficiency can be expected to be lower to that of a one-electron oxidation of Cu^I-tmpa or [Fe(CN)$_6$]$^{4-}$. Additionally, there is a significant phosphate buffer dependence present in the electrochemical oxidation of H$_2$O$_2$ by Pt.[5] While a significant effect is shown at high [H$_2$O$_2$] and low [PO$_4$], linear behaviour is observed with [PO$_4$] =100 mM in the low H$_2$O$_2$ concentration range.

The collection efficiency for hydrogen peroxide (N_{H2O2}) was determined by using a GC disk to generate H$_2$O$_2$ through the 2-electron reduction of O$_2$. As the Pt disk should be held at a potential where oxidation of H$_2$O$_2$ is mass-transport limited, CVs were measured on the Pt ring while rotating the RRDE setup at 1600 RPM in 1.5 mM H$_2$O$_2$ (pH 7 phosphate buffer, [PO$_4$] =100 mM). It was found that 1.2 V vs. RHE is within the H$_2$O$_2$ mass-transport limited regime under our experimental conditions (Figure A.10a).
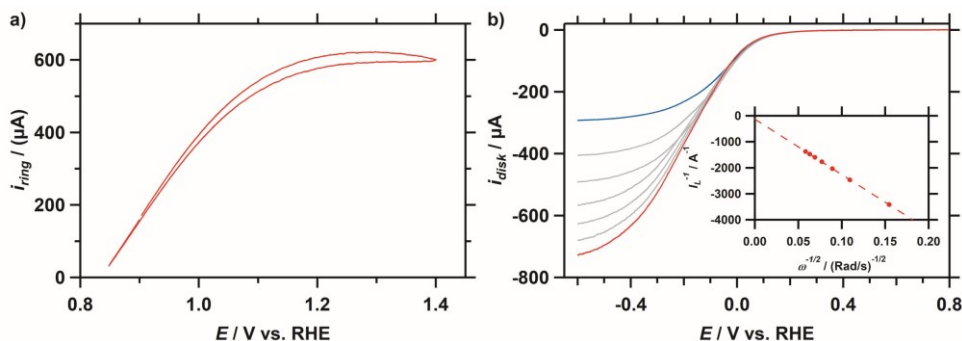
Figure A.10. a) CV measured at the Pt ring electrode in the presence of 1.5 mM H_2O_2. **b)** RDE LSVs of bare GC under 1 atm O_2 at different rotation rates from 400 RPM (blue line) to 2800 RPM (red line), 400 RPM increments. The inset shows the KL plot of the inverse limiting current (I_L^{-1}) at -0.6 V (vs. RHE.) as a function of the inverse square root of the rotation rate. Conditions: pH 7 PB ([PO_4] = 100 mM), 293 K, Pt ring at 1.2 V vs. RHE, 50 mV s^{-1} scan rate.

Secondly, the electron-transfer number of the ORR by GC under our conditions was established by performing a Koutecky-Levich analysis as previously described, resulting in n_{KL} = 2.04 (Figure A.10b). For a reliable N_{H2O2}, chronoamperometric (CA) measurements were performed by applying several different potentials to the GC disk at 1600 RPM, while the Pt ring was held at 1.2 V vs. RHE. The disk potential was first held at 0.8 V for 60 seconds, followed by a potential step to either 0.1, 0.0, or −0.1 V, which was held for 180 seconds. A background correction was applied to the resulting ring current by subtracting the current measured on the ring while the disk was held at 0.8 V. N_{H2O2} was calculated by taking i_{ring} over i_{disk}, and was shown to be stable as function of time and applied potential (Figure A.11). The final N_{H2O2} = 0.125 was obtained by averaging the values between t = 30 s and t = 60 s, and was used in further calculations.
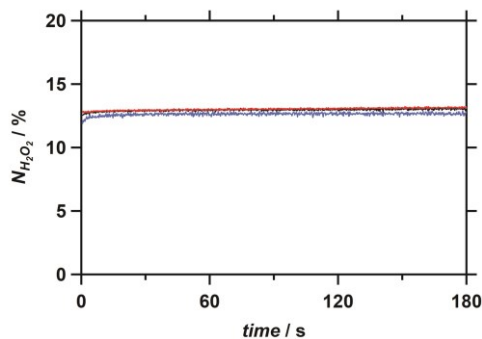

Figure A.11. Hydrogen peroxide collection efficiency (N_{H2O2}) determined from RRDE CA measurements of the ORR (1 atm O_2) by a GC disk performed at different E_{disk}: 0.1 (blue), 0.0 (black), and −0.1 V (red). Conditions: pH 7 PB ([PO_4] = 100 mM), 293 K, Pt ring at 1.2 V vs. RHE.

A.7 Quantification of H_2O_2 during the ORR by Cu-tmpa

The percentage H_2O_2 (%H_2O_2) produced as a function of applied potential was determined using similar RRDE CA measurements as described in the previous section. The CA measurements were performed by applying several different potentials to the GC disk at 1600 RPM in the presence of 0.3 mM Cu-tmpa, while the Pt ring was held at 1.2 V vs. RHE. First, E_{disk} was held at 0.8 V for 60 s, followed by a potential step to the desired potential, which was held for 300 s. The resulting current-response graphs are shown in Figure A.12a. A background correction was applied to the resulting i_{ring} by subtracting the current measured on the ring while the disk was held at 0.8 V. Additionally, a small background correction was applied to i_{disk} by subtracting the current measured at E_{disk} = 0.6 V (Figure A.12a, broken line). The resulting %H_2O_2 were shown to be stable over time (Figure A.12b). The final values of %H_2O_2 were obtained by averaging over a 30 s time interval and the resulting %H_2O_2 as a function of applied potential are shown in the main text (Figure 2.5). The electron transfer number n_{RRDE} that was obtained using the same data set is shown in Figure A.12c, by using Eq. A.4. A
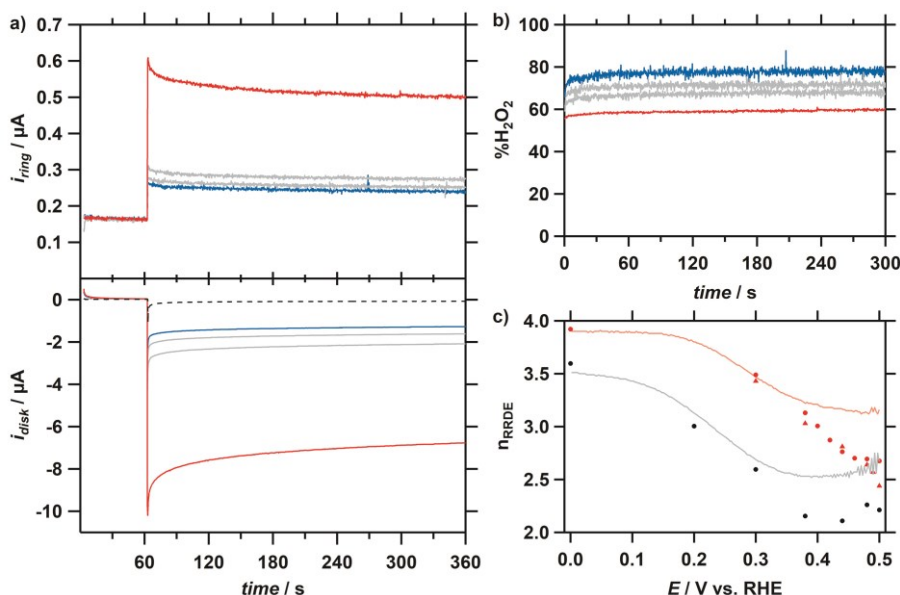

Figure A.12. a) RRDE CA measurements. E_{disk} at t = 0–60 s was held at 0.8 V vs RHE, followed by a potential step. Blue to red traces: 0.50, 0.49, 0.48, 0.44 V vs. RHE. **b)** %H_2O_2 obtained from RRDE CA measurements with 0.3 mM Cu-tmpa. **c)** n_{RRDE} obtained from RRDE CA (dots and triangles) and LSV (lines, 50 mV s^{-1}) measurements as a function of applied potential at a rotation rate of 1600 RPM with 0.3 mM (red), and 1.0 μM (black) Cu-tmpa. Conditions: pH 7 PB ([PO_4] = 100 mM), 293 K, Pt ring at 1.2 V vs. RHE.

duplicate experiment was performed and both datasets are plotted. For comparison %H_2O_2 and n_{RRDE} obtained from LSV (50 mV s^{-1}) are plotted in their relevant figures (Figure 2.5 and Figure A.12c). Significant underestimation of %H_2O_2 is shown during LSV measurements at potentials closer to the onset of the ORR, compared to CA measurements. The same measurements were also performed at a Cu-tmpa concentration of 0.1 µM (Figure A.13).

$$n_{RRDE} = \frac{4 \times i_{disk}}{i_{disk} + (i_{ring}/N_{H2O2})} \qquad (A.4)$$
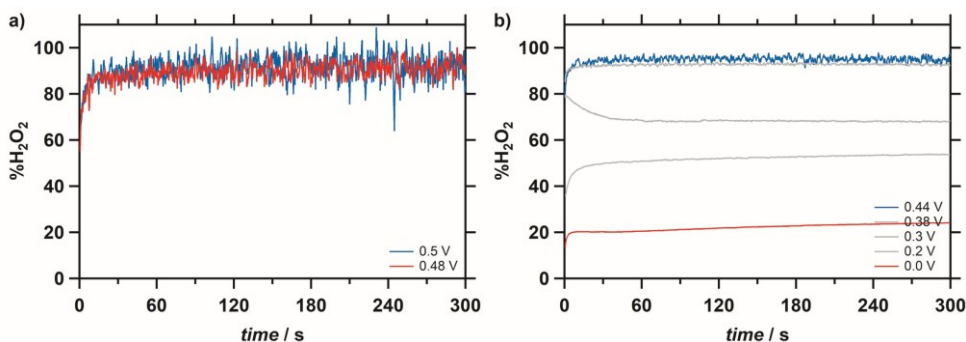

Figure A.13. %H_2O_2 obtained from RRDE CA measurements at a rotation rate of 1600 RPM. Conditions: pH 7 PB ([PO$_4$] = 100 mM), [Cu-tmpa] = 1.0 µM, 293 K, Pt ring at 1.2 V vs. RHE.

A.8 Comparison of O_2 and H_2O_2 reduction by Cu-tmpa

The onset potential of H_2O_2 reduction (0.45 V) is ca. 50 mV lower than that of O_2 reduction, where onset is defined as the potential where the current in the presence of substrate is 3 times larger than the current in the absence of substrate ($i_c/i > 3$).
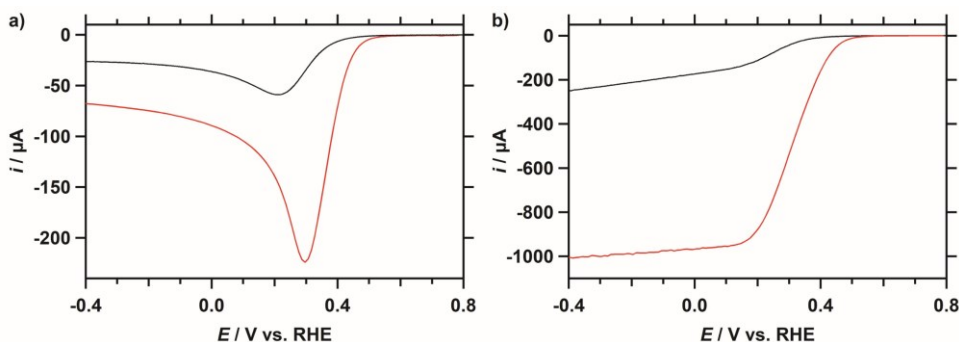

Figure A.14. LSVs of the reduction of 1 atm O_2 (red line) and 1.1 mM H_2O_2 (black line) by Cu-tmpa. a) No rotation, b) 1600 RPM. Conditions: pH 7 PB ([PO$_4$] = 100 mM), [Cu-tmpa] = 0.3 mM, 293 K, 50 mV s^{-1} scan rate.

A.9   Electrochemical kinetics measurements and calculations

The k_{obs} (or TOF) can be directly determined from the catalytic current enhancement via Eq. 2.2. However, this method has significant limitations for the ORR due to the previously mentioned O_2 mass-transport limitation, which makes achieving kinetic conditions difficult. As the catalytic current by Cu-tmpa is concentration-independent over a large concentration range, a useful, catalyst concentration-independent TOF can only be determined at low catalyst concentrations, where the catalytic current is not mass transport limited in O_2. Therefore, i_{cat} were obtained from CVs with catalyst concentrations in the range of 0.1–1.0 µM. As no redox current can be observed at these low concentrations, the corresponding i_p values were calculated through the Randles-Sevcik equation, using the previously calculated diffusion coefficient of Cu-tmpa. Thus, the current enhancement and TOF values were obtained by using the peak reductive current i_p calculated from the diffusion coefficient of Cu-tmpa (D = 4.9×10^{-6} cm^2/s). The measurements to obtain the catalytic current i_{cat} are described in section A.3. A plot of log(TOF) against the Cu-tmpa concentration is shown in Figure A.16, revealing that the TOF is independent of catalyst concentration. The TOF values were averaged over the concentration range and reported with the standard error.
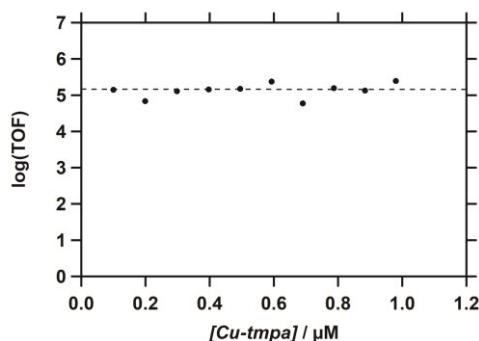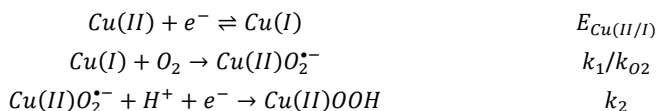

Figure A.15. Log(TOF) as a function of catalyst concentration. Conditions: pH 7 PB ([PO$_4$] = 100 mM), 293 K, 100 mV s^{-1} scan rate.

To investigate the kinetics of the electrocatalytic ORR by Cu-tmpa, we need to know which current-potential relationship applies to the catalytic system. The initial elemental steps involved in the reaction can be described as shown below, followed by consecutive (coupled) protonation and electron transfer steps.

$$Cu(II) + e^- \rightleftharpoons Cu(I) \qquad\qquad E_{Cu(II/I)}$$
$$Cu(I) + O_2 \rightarrow Cu(II)O_2^{\bullet-} \qquad\qquad k_1/k_{O2}$$
$$Cu(II)O_2^{\bullet-} + H^+ + e^- \rightarrow Cu(II)OOH \qquad\qquad k_2$$

FOWA only provides information about the first chemical step following the reduction of the catalyst[6], and previous studies[7] on the ORR of Cu-tmpa in aqueous solution have shown no dependence of the peak catalytic current on the pH of the solution (and thus the proton concentration). When the rate is independent of proton concentration, the reaction is only limited by O_2 binding and $k_{obs} = k_{O2}[O_2]$. Thus, the reaction can be simplified to an EC' type mechanism. So while the ORR is a much more complicated multielectron, multistep reaction, for the purpose of the FOWA the current-potential approximation as derived by Savéant et al[8-9] for an EC' type catalytic mechanism can be used for the electrochemical kinetics calculation (Eq. A.5). All electron transfer steps are considered to occur at the electrode, and no homogeneous electron transfer takes place between species.

$$i_c = \frac{nFSC_{cat}^0 \sqrt{D_{cat} k_{obs}}}{1 + exp\left[\frac{F}{RT}\left(E - E_{1/2}\right)\right]} \tag{A.5}$$

Where F is the faradaic constant, S the surface area of the catalyst, C_{cat}^0 the bulk catalyst concentration, D_{cat} the diffusion coefficient of the catalyst, $E_{1/2}$ the equilibrium potential of the catalyst redox couple, and k_{obs} the observed rate constant, with $k_{obs} = TOF_{max}$. Eq. A.5 can be normalized with the peak current of the one-electron reduction of the catalyst (i_p) using the Randles-Sevcik equation (Eq. A.6), resulting in Eq. A.7.

$$i_p = 0.446nFSC_{cat}^0 \sqrt{\frac{Fv}{RT} D_{cat}} \tag{A.6}$$

$$\frac{i_c}{i_p} = \frac{2.24n \sqrt{\frac{RT}{Fv} k_{obs}}}{1 + exp\left[\frac{F}{RT}\left(E - E_{1/2}\right)\right]} \tag{A.7}$$

Where n is the number of electrons used in the catalytic cycle, which in this specific case is 2, considering only the partial reduction of O_2 to H_2O_2 in the FOWA region. As a plateau current is not reached, the analysis can only be applied at the foot of the catalytic wave, where no side-phenomena take place. We also note that the half-wave potential of the catalytic wave $E_{cat/2} > E_{1/2}$ due to substrate depletion near the electrode. As $exp[F/RT\left(E - E_{1/2}\right)] \gg 1$ in this potential window, Eq. A.7 can be simplified to Eq. A.8. Using Eq. A.8, k_{obs} can be derived from the slope of i_c/i_p vs. $exp\left[-F/RT\left(E - E_{1/2}\right)\right]$.

$$\frac{i_c}{i_p} = 2.24n \sqrt{\frac{RT}{Fv} k_{obs}} \, exp\left[-\frac{F}{RT}\left(E - E_{1/2}\right)\right] \tag{A.8}$$

Mechanistic insight can be obtained from FOW analysis. In case of a first order relationship in catalyst, the catalytic current should be linear with $1 + exp[F/RT\,(E - E_{1/2})]$, while for a homolytic second order reaction the catalytic current should be linear with $(1 + exp[F/RT\,(E - E_{1/2})])^{3/2}$.[8] When the current-potential relationship for a binuclear homolytic reaction were applied, very poor linearity was observed. Thus, plots of i_c/i_p vs. $exp[F/RT\,(E - E_{1/2})]$ were fitted linearly between the onset of the ORR, here defined as $i_c/i_{redox} \geq 2$, and 0.38 V vs. RHE. Here, i_{redox} is the current of the catalyst measured at the applied potential, in the absence of O_2 (Figure A.17). Measurements were repeated five times and FOWA was performed on the individual measurements. Averaging of the results obtained for the individual experiments led to the TOFs as reported with the standard error.
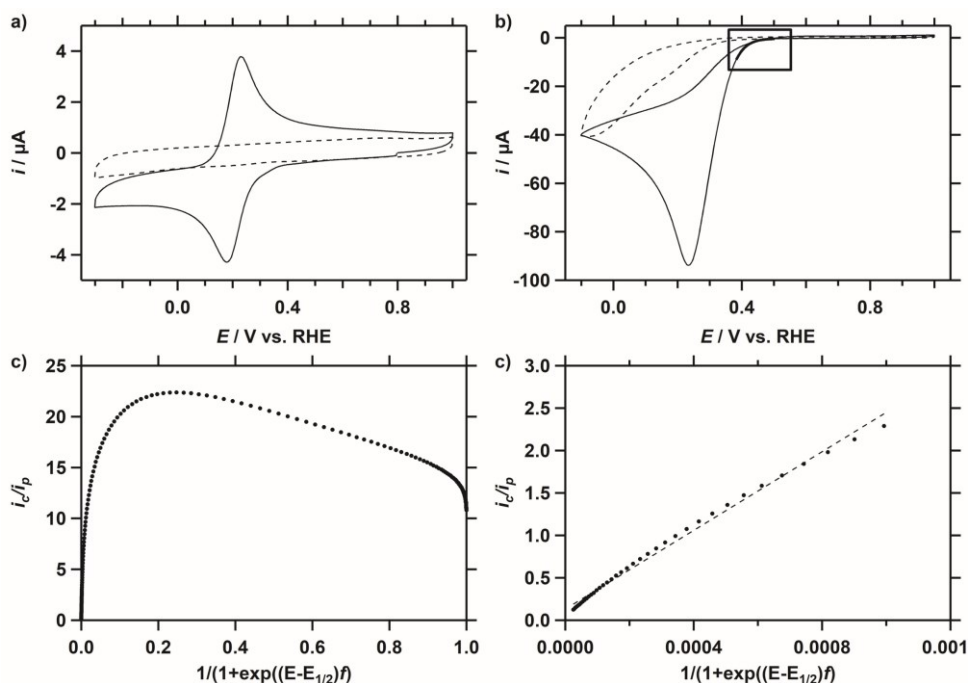

Figure A.16. a) CV of bare GC electrode (dotted line) and Cu-tmpa under 1 atm Ar. **b)** CV of bare GC electrode (dotted line) and Cu-tmpa under 1 atm (O_2). **c)** FOW analysis of Cu-tmpa, where $f = F/RT$. **d)** Fit of the linear region of the FOW analysis, $R^2 = 0.99$. Conditions: pH 7 phosphate buffer ([PO_4] = 100 mM), [Cu-tmpa] = 0.3 mM, 293 K, 100 mV s^{-1} scan rate.

A.10   References

[1]   H. Taube, *Chem. Rev.* **1952**, *50*, 69-126.

[2]   D. T. Richens, *Chem. Rev.* **2005**, *105*, 1961-2002.

[3]   B. van Dijk, J. P. Hofmann, D. G. H. Hetterscheid, *Phys. Chem. Chem. Phys.* **2018**, *20*, 19625-19634.

[4]   R. Zhou, Y. Zheng, M. Jaroniec, S.-Z. Qiao, *ACS Catal.* **2016**, *6*, 4720-4728.

[5]   S. B. Hall, E. A. Khudaish, A. L. Hart, *Electrochim. Acta* **1999**, *44*, 4573-4582.

[6]   E. S. Rountree, B. D. McCarthy, T. T. Eisenhart, J. L. Dempsey, *Inorg. Chem.* **2014**, *53*, 9983-10002.
[7]   M. Asahi, S.-i. Yamazaki, S. Itoh, T. Ioroi, *Electrochim. Acta* **2016**, *211*, 193-198.
[8]   C. Costentin, J.-M. Savéant, *ChemElectroChem* **2014**, *1*, 1226-1236.
[9]   C. Costentin, S. Drouet, M. Robert, J.-M. Savéant, *J. Am. Chem. Soc.* **2012**, *134*, 11235-11242.

Appendix B

Supplementary Information for Chapter 2

B.1   Catalyst concentration dependence studies

To determine the peak catalytic current i_{cat} at low Cu-tmpa concentrations, the GC working electrode was polished before every catalytic measurement using a Struers LaboPol-30 polishing machine, using 1.0 µm diamond and 0.04 µm silica suspension on polishing cloths (Dur-type) for 1 min each. This was followed by sonication for 10 to 15 minutes in Milli-Q purified water. A similar process was followed for the experiments in D_2O, as described in the Experimental section of Chapter 3. A blank CV was measured in a separate electrochemical cell by the GC electrode in an Ar saturated (1 atm) solution after every electrode polish to determine the quality of the polish and the size of the double layer. Fresh solutions containing Cu-tmpa and 1.1 mM H_2O_2 were used for every incremental increase of catalyst concentration. The currents obtained from CV measurements in presence of Cu-tmpa were corrected using their corresponding blank measurement, giving the catalytic current without any contribution from the double layer of the GC electrode to the catalytic current of the HPRR by Cu-tmpa.
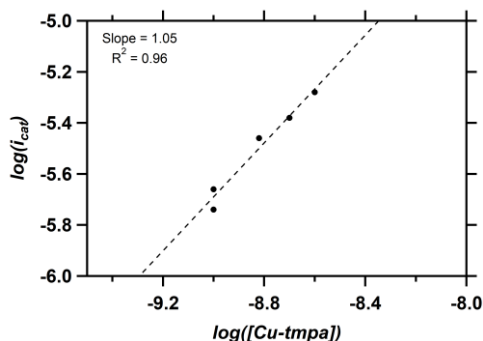

Figure B.1. Log-log plot of the i_{cat} (in A) vs. the Cu-tmpa concentration (in M) to determine the linearity of the dependence of the HPPR on Cu-tmpa, in the presence of 1.1 mM H_2O_2. The slope of the fit is 1.05 (R^2 = 0.96).
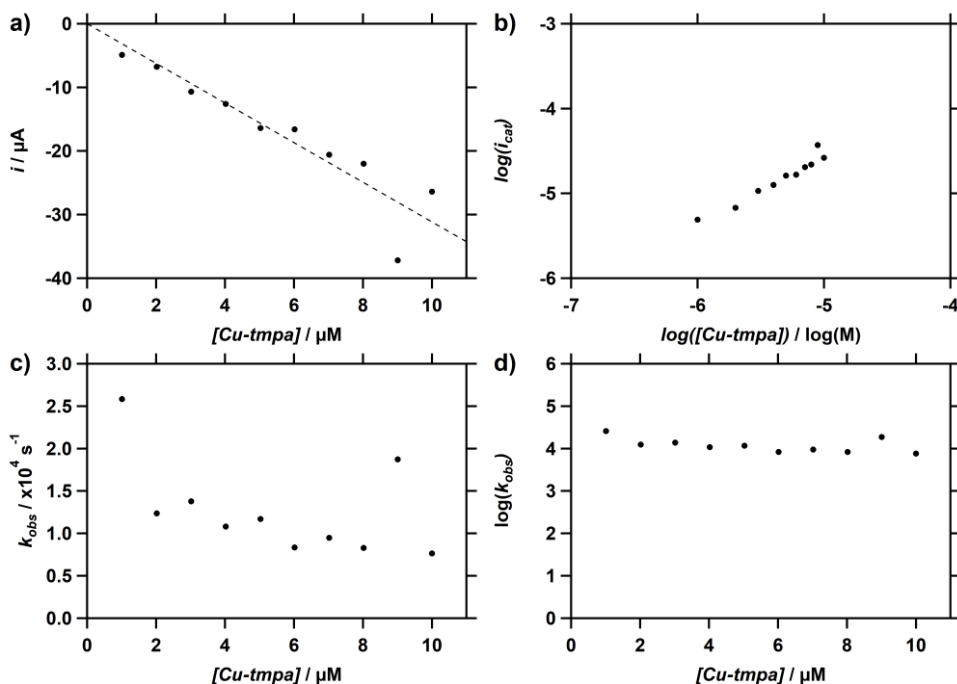
Figure B.2. a) Background corrected catalytic current i_{cat} as a function of Cu-tmpa concentration with 10 mM H_2O_2. **b)** Log-log plot of the same data. **c)** k_{obs} of the reduction of H_2O_2 as a function of Cu-tmpa concentration with 10 mM H_2O_2. **d)** Log(k_{obs}) as a function of catalyst concentration. Conditions: pH 7 PB ([PO_4] = 100 mM), 293 K, 100 mV s^{-1} scan rate.

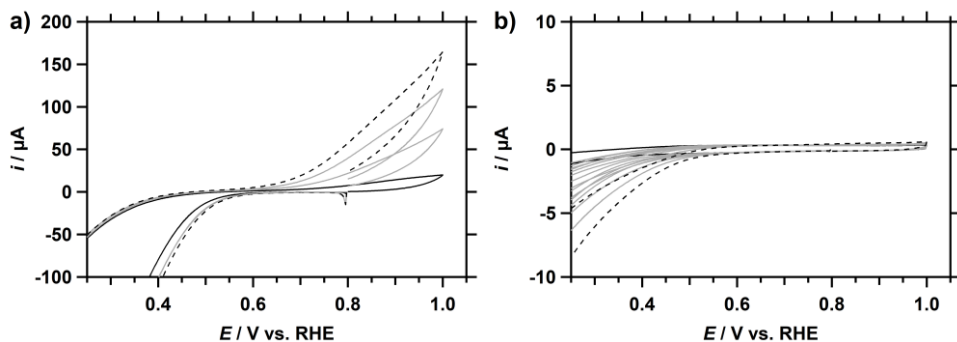## B.2   Catalytic oxidation at high H_2O_2 concentrations

Figure B.3. a) Zoom of the observed oxidation during cyclic voltammetry measurements of the reduction of H_2O_2 in the presence of 0.3 mM Cu-tmpa for a range of H_2O_2 concentrations; 40 (solid black)/60/80/100 (dashed) mM. **b)** CVs of a GC electrode in electrolyte solutions containing 1.5 (solid black) to 500 (dashed) mM H_2O_2. Conditions: pH 7 PB ([PO_4] = 100 mM), 293 K, 100 mV s^{-1} scan rate.

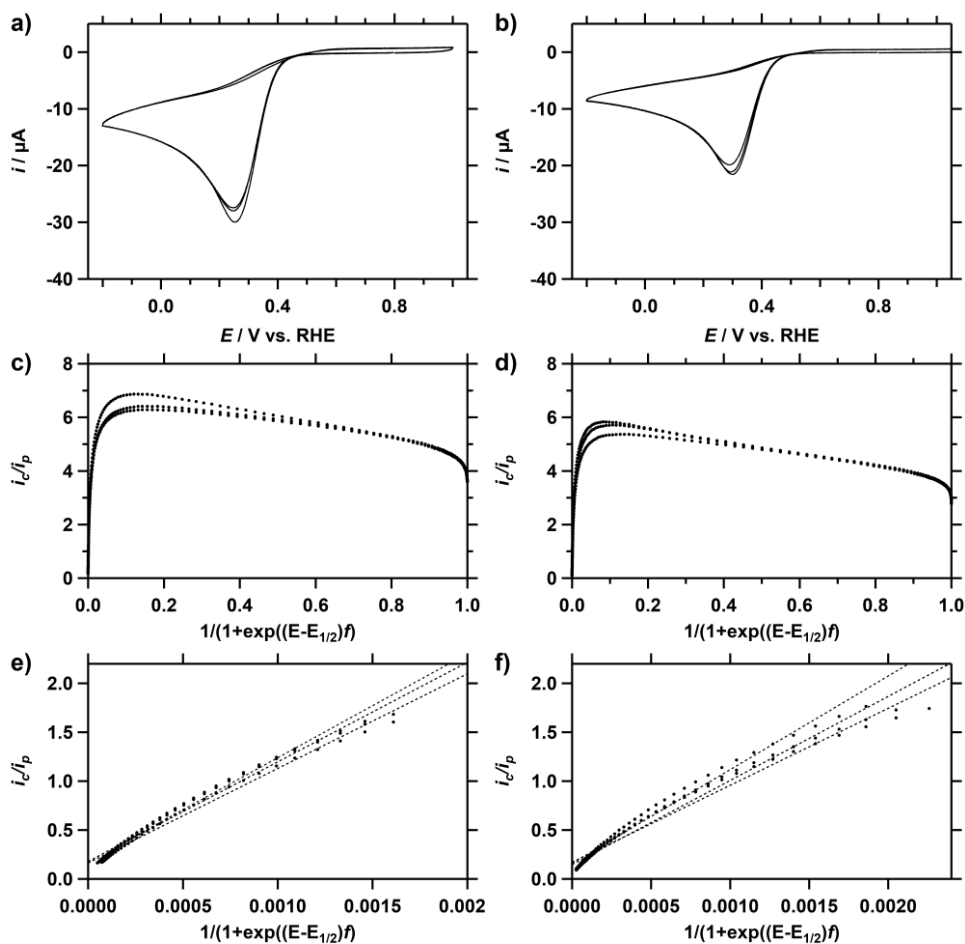## B.3 FOWA of the HPRR in deuterated and non-deuterated solutions

Figure B.4. Triplicate CVs of the reduction of 1.1 mM H_2O_2 in the presence of 0.3 mM Cu-tmpa in non-deuterated **(a)** and deuterated **(b)** PB electrolyte solutions under 1 atm Ar. FOWA of the HPRR for non-deuterated **(c)** and deuterated **(d)** conditions, where $f = F/RT$. Corresponding fits of the linear regions of the FOWA for non-deuterated **(e)** and deuterated **(f)** conditions, $R^2 \geq 0.98$. Conditions: pH 7 PB ([PO_4] = 100 mM), 293 K, 100 mV s^{-1} scan rate.
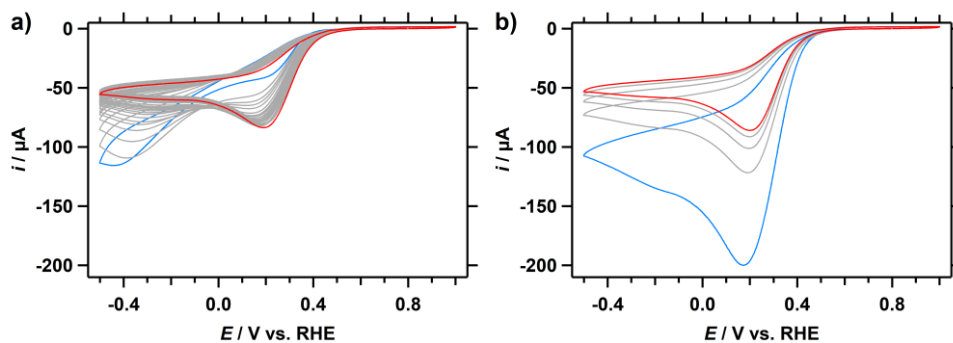
B.4   Stability of Cu-tmpa in H₂O₂

Figure B.5. a) CVs showing 25 consecutive scans of the catalytic reduction of H₂O₂ (10 mM) by Cu-tmpa (8.0 µM) under 1 atm Ar. A clear increase in catalytic current is observed with each scan, from the first scan (blue) to the last scan (red). **b)** CVs of the same solution after mixing and saturating the solution for 1 min with 1 atm Ar, while keeping the electrode submerged in the solution. A large initial catalytic current is observed as the H₂O₂ near the electrode has been replenished by mixing, indicating a deposition has formed on the electrode during the experiment shown in (**a**). Conditions: pH 7 PB ([PO₄] = 100 mM), 293 K, 100 mV s⁻¹ scan rate.

Appendix C

Supplementary Information for Chapter 4
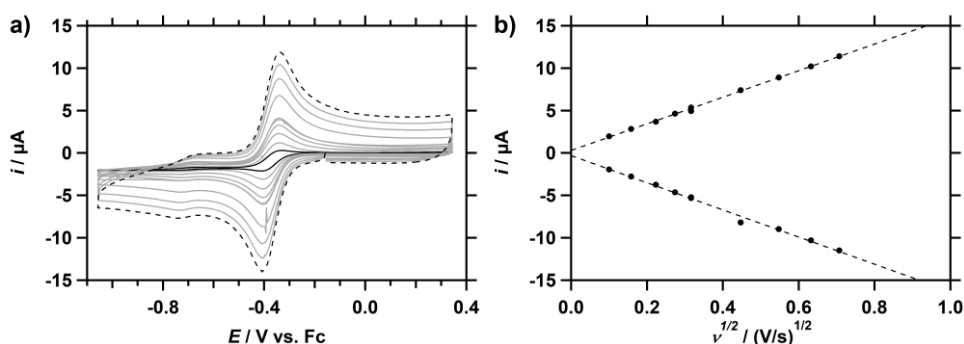
C.1   Scan rate dependence

Figure C.1. a) CVs of Cu-tmpa (0.3 mM) in an electrolyte solution under argon at a range of different scan rates (10-500 mV s^{-1}). **b)** The resulting Randles-Sevcik plot of i_{pc} and i_{pa}. Conditions: NBu$_4$PF$_6$ (100 mM) in MeCN, 293 K.

The reported diffusion coefficients in Table C1 were determined using the Randles-Sevcik equation and are based on the peak reductive (cathodic) current i_{pc} as this corresponds the diffusion coefficient of Cu^{II}-tmpa, the species that has to diffuse to the electrode. This distinction is especially important when the cathodic and anodic peak current show very different slopes as a function of scan rate. Due to the overlapping redox events, no diffusion coefficients were determined for Cu-tmpa in solutions containing HNEt$_3^+$ or HNEt$_3^+$/NEt$_3$ mixtures (Figure C.2e/f).

Table C.1. Overview of diffusion coefficients of Cu-tmpa with different additives in the electrolyte

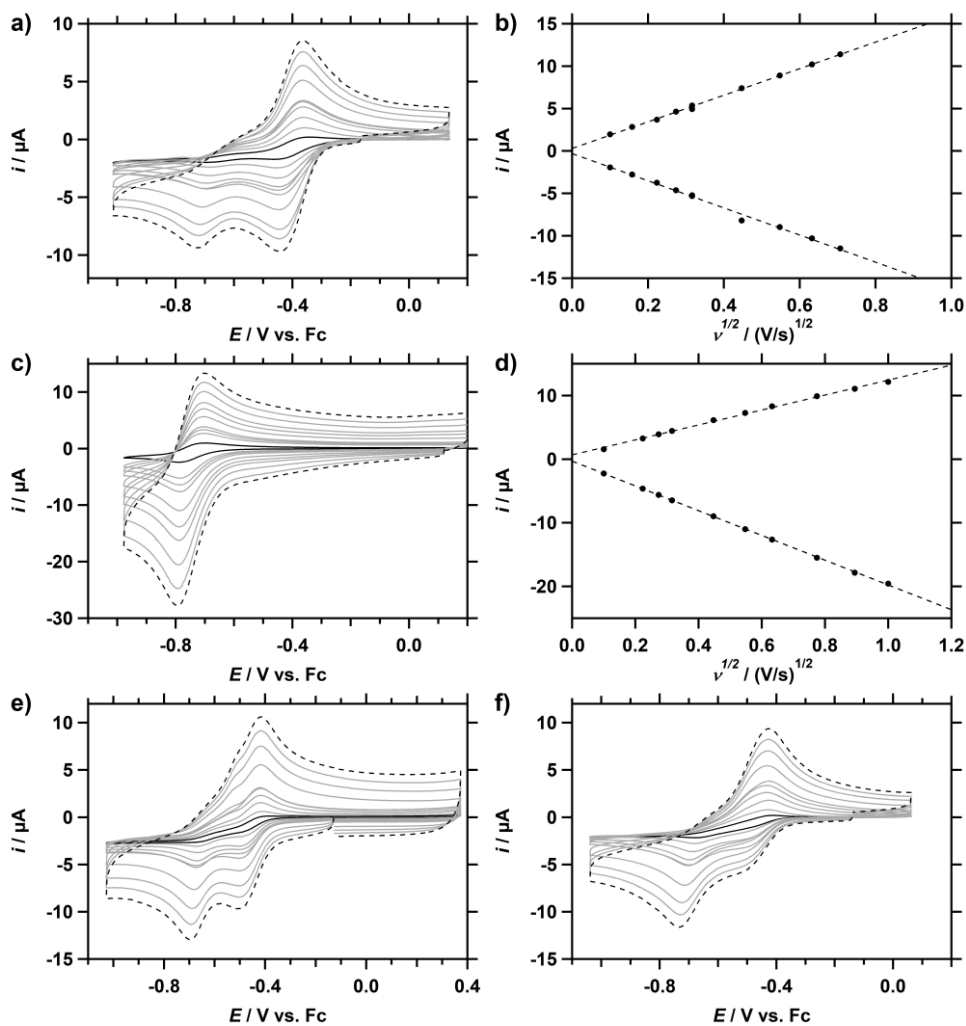| Conditions	D$_{red}$ (cm^2 s^{-1})
No Acid	7.8×10^{-6}
HOAc	4.4×10^{-6}
HOAc/OAc$^-$	11.5×10^{-6}

Figure C.2. CVs of Cu-tmpa (0.3 mM) in an electrolyte solution under argon containing different acid or acid-conjugate base mixtures. **a)** HOAc (100 mM) and **(b)** the corresponding Randles-Sevcik plot. **c)** HOAc/OAcNBu$_4$ (20 mM each) and **(d)** the corresponding Randles-Sevcik plot. **e)** HNEt$_3$PF$_6$ (60 mM). **f)** HNEt$_3$PF$_6$/NEt3 (50 mM each). Conditions: NBu$_4$PF$_6$ (100 mM) in MeCN, 293 K.
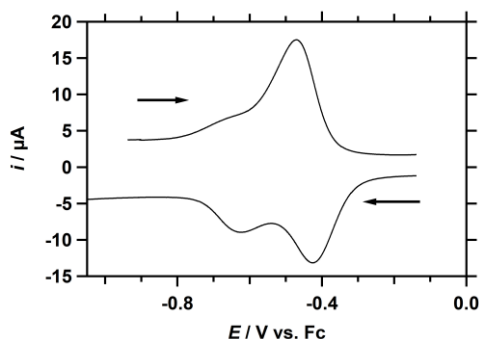
C.2 DPV measurements

Figure C.3. Differential pulse voltammetry (DPV) measurements of Cu-tmpa (0.3 mM) in an electrolyte solution containing buffered HNEt$_3$PF$_6$/NEt$_3$ acid-conjugate base mixture (50 mM each) in the presence of 1 atm Ar. Conditions: NBu$_4$PF$_6$ (100 mM) in MeCN, 293 K.

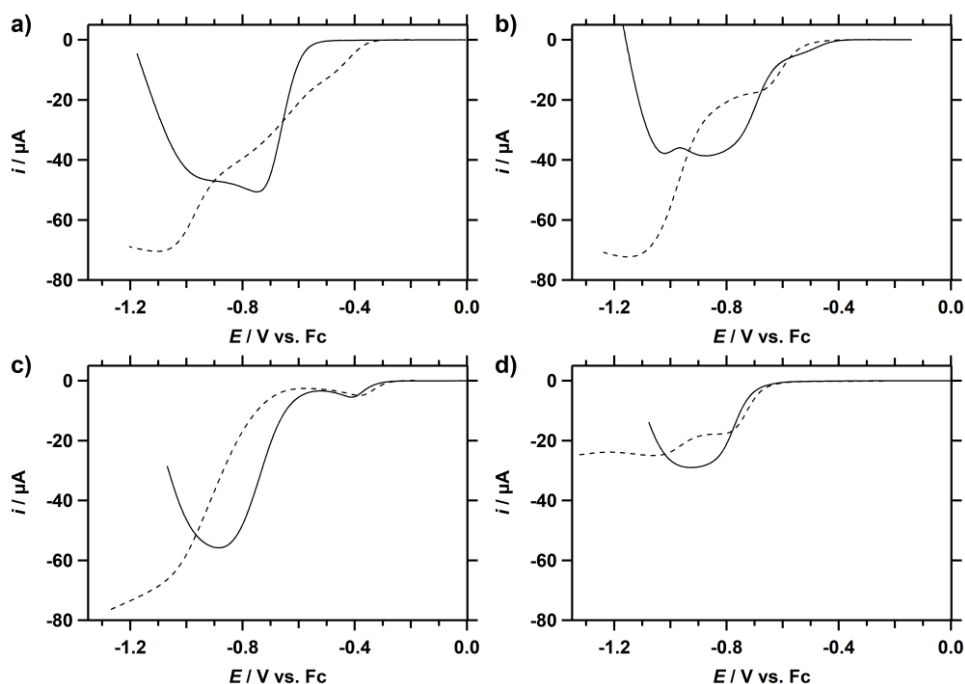## C.3 Comparison of the ORR and HPRR in different conditions

Figure C.4. Background-corrected LSVs of the ORR (solid line) and HPRR (dotted line), by Cu-tmpa in the presence of **(a)** 50 mM HNEt$_3$PF$_6$, **(b)** 50 mM HNEt$_3$PF$_6$/NEt$_3$, **(c)** 20 mM HOAc, and **(d)** 20 mM HOAc/OAc$^-$. Conditions: NBu$_4$PF$_6$ (100 mM) in MeCN, 100 mV s^{-1}, 293 K.
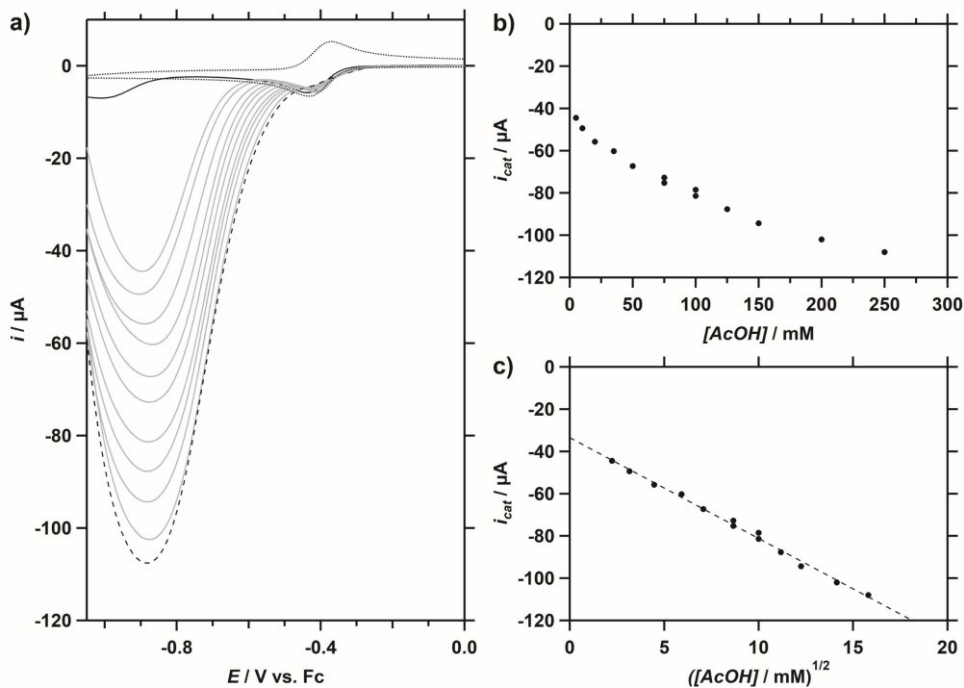
C.4   Acetic acid concentration dependence studies

Figure C.5. a) Background-corrected LSV of the ORR by Cu-tmpa (0.3 mM) in the presence of 0 (solid line) to 250 mM (dashed line) of HOAc, under 1 atm O_2. Redox couple under 1 atm Ar and 0 mM HOAc included as reference. **b)** The peak catalytic current i_{cat} plotted against [HOAc]. **(c)** The peak catalytic current i_{cat} plotted against the square root of [HOAc]. Conditions: NBu_4PF_6 (100 mM) in MeCN, 1 atm O_2, 100 mV s^{-1}, 293 K.

The ORR catalysed by Cu-tmpa in a NBu_4PF_6 (100 mM in MeCN) electrolyte solution containing HOAc was further studied by extending the concentration range of HOAc. Cyclic voltammograms in solutions containing 0.3 mM Cu-tmpa and 0 to 250 mM HOAc were measured with a glassy carbon electrode, freshly polished after each catalytic measurement. CVs were also measured in solutions using the same concentrations of acid without catalyst present to obtain the background current of the GC electrode towards the ORR. Background correction of the catalytic measurements resulted in the LSV shown in Figure C.5a. In Figure C.5b, the peak catalytic current i_{cat} is shown versus the HOAc concentration, where it is shown that it does not increase linearly with increasing acid concentration. Additionally, when a plot of the catalytic current against the square root of the concentration is constructed, a perfectly linear relationship ($R^2 > 0.99$) is visible. Following Eq. 3.3, i_{cat} is a function of the square root of the observed rate constant k_{obs}, and as a linear relationship between i_{cat} and the square

root of the acid concentration is present, k_{obs} can be defined as shown in Eq. C.1, while Eq 3.3 can be rewritten as Eq. C.2.

$$k_{obs} = k[AcOH] \qquad (C.1)$$

$$\frac{i_{cat}}{i_p} = 2.24n\sqrt{\frac{RT}{Fv}k[AcOH]} \qquad (C.2)$$

However, as was discussed in section 4.2.6 of Chapter 4, the redox current decreases as a function of increasing HOAc concentration. This effect can not only be seen under non-catalytic conditions (Figure 4.7a, Chapter 4), but also in the presence of 1 atm O_2, as shown in a zoom of the catalytic LSV (Figure C.6a). When calculating the k_{obs} as described in section 4.2.8, Chapter 4, using the corresponding i_p at −0.41 V for each different acid concentrations, a linear relationship between the TOF and acid concentration is observed. This type of linear dependency of the TOF on the acid concentration is indicative of a first-order in [HOAc], when the catalytic rate shows a first order dependency on the catalyst concentration. As a first order relationship of the catalysis on the catalyst concentration was indeed observed (section 4.2.7), this confirms the above hypothesis and would result in $r \approx k[HOAc][Cu]$ as the rate equation for the ORR.
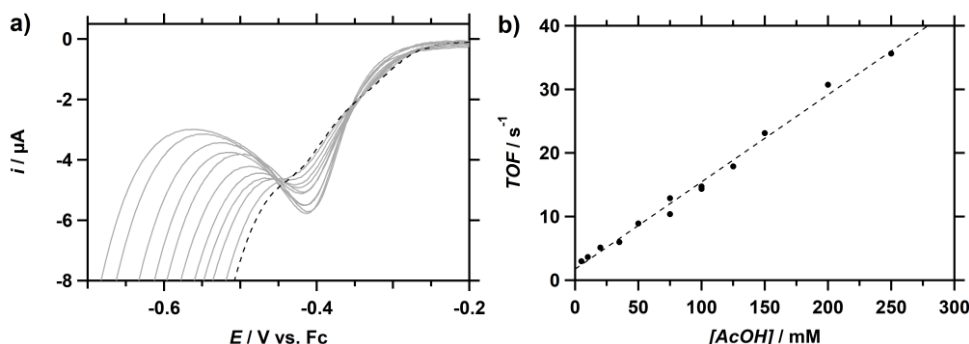

Figure C.6. a) Zoom of the background-corrected LSV of the ORR by Cu-tmpa in the presence of 1 atm O_2 for different concentrations of HOAc, ranging from 5 mM (blue trace) to 100 mM (red trace). **b)** The resulting TOF (k_{obs}) as a function of acid concentration. Conditions: NBu$_4$PF$_6$ (100 mM) in MeCN, 100 mV s^{-1}, 293 K.

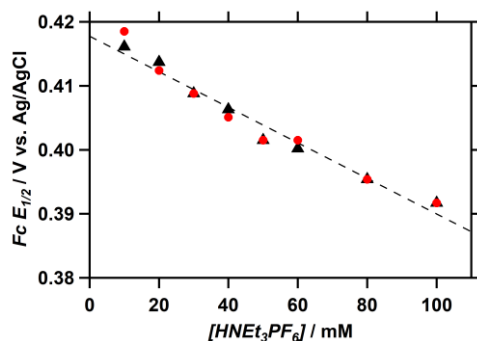## C.5 Shift of the Fc redox couple as a function of [HNEt₃PF₆]

Figure C.7. Shift of the $E_{1/2}$ of Fc as a function of $HNEt_3^+$ concentration, in the presence (red) and absence (black) of 0.3 mM Cu-tmpa. Conditions: NBu₄PF₆ (100 mM) in MeCN, 100 mV s⁻¹, 293 K.

C.6 Stability of the Ag/AgNO₃ reference electrode over time

As AgNO₃ is photosensitive, the stability of the Ag/AgNO₃ electrode was monitored. When an Ag/AgNO₃ reference electrode was used during measurements and the Fc (0.6 mM) redox couple was measured as the reference, a shift of the $E_{1/2}$ of the Fc redox couple was observed over the course of multiple experiments (Figure C.8). At the same time, a reduction in the solvent level in the outer junction and to a lesser degree the inner junction was observed. Both evaporation and leaking of the MeCN electrolyte through the diaphragm may have played a role. Repeated cleaning and refilling resulted in the same behaviour, highlighting the importance of measuring the Fc redox couple with every experiment. This issue was not observed with the reference electrode was used with Ag/AgCl, as the higher surface tension of H₂O decreases evaporation and diffusion through the diaphragm of the electrode.
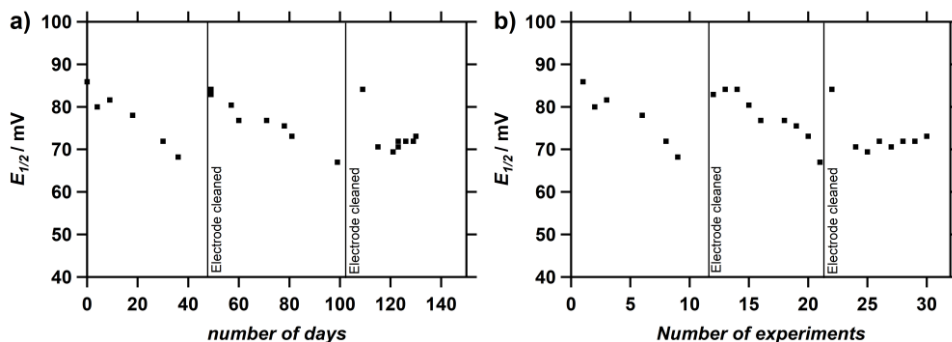

Figure C.8. The $E_{1/2}$ of the redox couple of Fc⁺/Fc, measured with an Ag/AgNO₃ reference electrode. **a)** plotted against the time between experiments. **b)** plotted against the number of conducted experiments. Conditions: NBu₄PF₆ (100 mM) in MeCN, 293 K.

C.7 Determination of species distribution

In the case of a solution containing two different redox-active species, the current measured at a given potential is a linear combination of the redox current associated with the individual species at this given potential. Thus, the current at any given reduction or oxidation potential can be described by Eq. C.3 and Eq. C.4, where the fraction of species 1 is given by $x_1 = [1]/[Cu]_{tot}$ and the fraction of species 2 is given by $x_2 = [2]/[Cu]_{tot}$. The potentials E1 and E2 were chosen at positions where the difference between the measured redox currents is greatest, as visualized in Figure C8a. If species 1 is not present in the solution, the reductive current at potential E1 (i_{red}^{E1}) should be close to zero, while if species 2 is not present in the solution, the oxidative current at potential E2 (i_{ox}^{E2}) should approach zero.

$$i_{red}^{E1} = x_1 \times i_{red,[1]}^{E1} + x_2 \times i_{red,[2]}^{E1} \qquad (C.3)$$

$$i_{ox}^{E2} = x_1 \times i_{ox,[1]}^{E2} + x_2 \times i_{ox,[2]}^{E2} \qquad (C.4)$$

Eq. C.3 can be rewritten as an expression of x_1

$$x_1 = \frac{i_{red}^{E1} - x_2 \times i_{red,[2]}^{E1}}{i_{red,[1]}^{E1}} \qquad (C.5)$$

Eq. C.5 can be inserted into equation C.4 and solved for x_2, while the same treatment can be done for x_1.

$$x_2 = \frac{i_{ox}^{E2} \times i_{red,[1]}^{E1} - i_{red}^{E1} \times i_{ox,[1]}^{E2}}{i_{red,[1]}^{E1} \times i_{ox,[2]}^{E2} - i_{ox,[1]}^{E2} \times i_{red,[2]}^{E1}} \qquad (C.6)$$

$$x_1 = \frac{i_{ox}^{E2} \times i_{red,[2]}^{E1} - i_{red}^{E1} \times i_{ox,[2]}^{E2}}{i_{ox,[1]}^{E2} \times i_{red,[2]}^{E1} - i_{red,[1]}^{E1} \times i_{ox,[2]}^{E2}} \qquad (C.7)$$

The total copper concentration in the solution $[Cu]_{sol}$ at a given time can be calculated using x_1 and x_2 derived in the previous section.

$$[Cu]_{sol}(t) = x_1(t) \times [Cu]_{start} + x_2(t) \times [Cu]_{start} \qquad (C.8)$$

Application of Eq. 8 resulted in Figure C.9b, where an increasing copper concentration is observed, which coincides with the observed solvent evaporation over the course of the experiment. Despite saturating the Ar flow with MeCN before passing it through the electrochemical cell, 1.2 mL out of 5 mL (24%) of the MeCN evaporated over the course of the 6-hour experiment, as confirmed after experiment completion. Normalizing the [Cu]sol at every point in time to account for this evaporation of solvent is required to obtain the actual species distribution (Figure C9c). Alternatively, a linear rate of evaporation as a function of time between start and endpoint of the experiment

can be assumed, considering the constant flow rate of Ar and the constant surface area of the solution exposed to the Ar flow. Little deviation of the results from either method was observed.
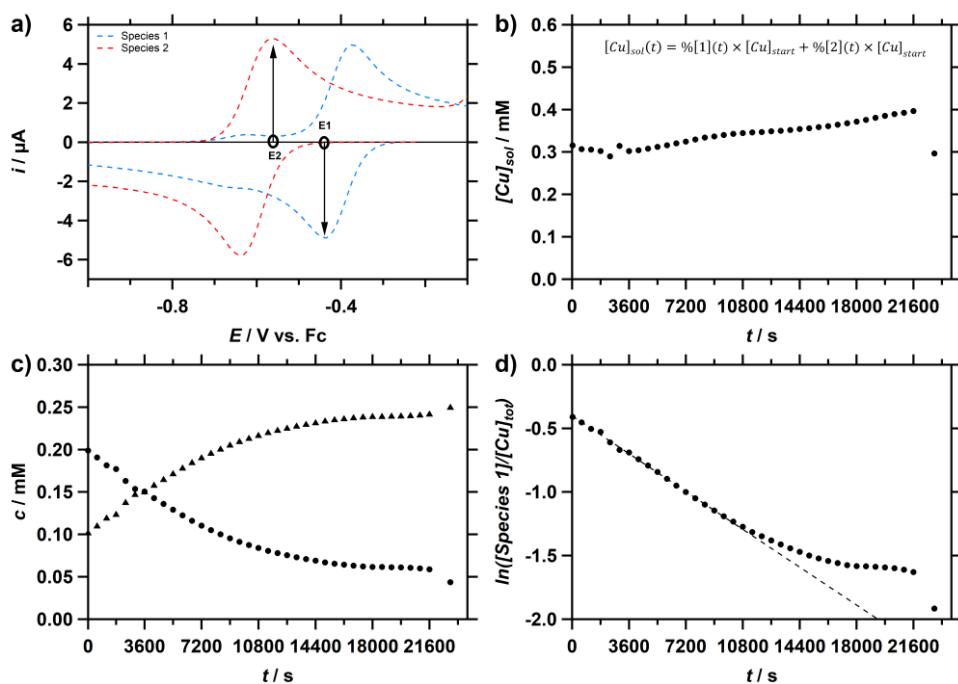

Figure C.9. a) CV of Cu-tmpa (0.3 mM) in the presence of 1 atm Ar and 100 mM HNEt$_3$PF$_6$ (red trace) or no acid (blue trace) showing the positions of E1 and E2 for the determination of species distribution during the time-dependent conversion. **b)** Cu-tmpa concentration change as a function of time, showing the evaporation of MeCN during the experiment. **c)** Change in concentration of both species present in solution as a function of time. **d)** Plot of the natural logarithm of the initial species present in solution versus time. The reaction rate constant was determined from the slope of the linear fit. Conditions: NBu$_4$PF$_6$ (100 mM) in MeCN, 100 mV s^{-1}, 293 K.
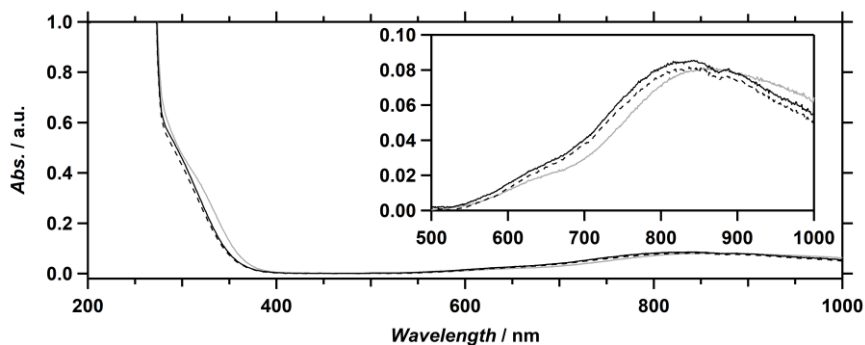
C.8 UV-vis time series measurements

Figure C.10. UV-vis absorption spectra of an electrolyte solution containing 0.30 mM Cu-tmpa, 0.10 M NBu$_4$PF$_6$ in MeCN, without acid (grey trace) or with 50 mM HNEt$_3$PF$_6$ (dashed trace). The solid black trace was measured 360 min after addition of the acid. Insert: zoom of the d–d transition band.

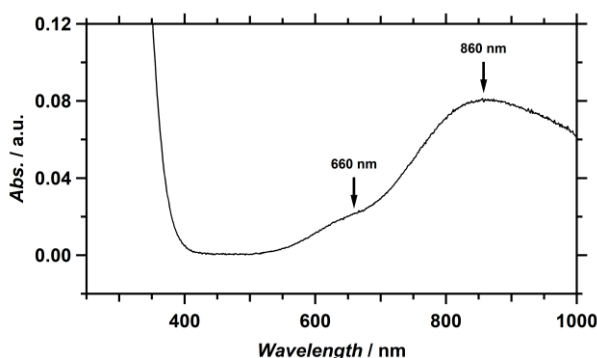## C.9 Absorption spectra and stability of Cu-tmpa in electrolyte solutions

Figure C.11. UV-vis absorption spectrum of an electrolyte solution containing 0.30 mM [Cu^{II}(tmpa)(CH$_3$CN)]$^{2+}$ and 0.10 M NBu$_4$PF$_6$ in MeCN at 293 K.

The UV-vis absorption spectrum of [Cu^{II}(tmpa)(CH$_3$CN)]$^{2+}$ in MeCN, in the presence of 100 mM NBu$_4$PF$_6$ (Figure C.11) shows the characteristic absorption bands at 860 (ε = 260 M^{-1} cm^{-1}) and 660 nm in the d–d transition region, in good agreement with previously reported UV-vis spectra (in MeCN at RT).[1-2] This confirms that Cu-tmpa is present as a monomeric species in the resting state under these conditions.

To further study the stability of [Cu^{II}(tmpa)(CH$_3$CN)]$^{2+}$ and the possibility of adduct formation in the electrolyte solution used in this work, UV-vis absorption spectra were measured (Figure C.12). For each solution containing 0.30 mM Cu-tmpa, a CV was measured 30 seconds and 22 hours after addition of either the acid, acid-conjugate base mixture, or after addition of 8.1 mM H$_2$O$_2$. No change in the UV-vis spectra is

observed in the presence of HOAc or HNEt$_3^+$, neither upon addition of H$_2$O$_2$ to solutions containing these acids. In the presence of the acid-conjugate HNEt$_3^+$/NEt$_3$ mixture, a slight blue-shift of the main d–d absorption by 25 nm is observed. In the presence of HOAc/OAc$^-$ a clear change is observed in the UV-vis absorbance, especially in the lower wavelenghts. A new sharp absorption band at 299 nm appears, while at the same time the bands in the d–d region shift from 860 to 920 nm and from 660 to 720 nm. Additionally, an increase in absorbance is observed for the higher energy d–d band. Combined with the large change in redox potential (see main text),[3] this points to the formation of [Cu^{II}(tmpa)(OAc)]$^+$, with the 299 nm being the result of the AcO$^-$ → Cu ligand-to-metal charge transfer (LMCT) transition.

When H$_2$O$_2$ is added to a solution containing HOAc/OAc$^-$, an absorption band appears at 405 nm after 22 hours, while the d–d energy transitions are simultaneously decreased, indicating a loss of complex. Cu^{II} complexes, including [Cu^{II}(tmpa)]$^{2+}$, are known to react with H$_2$O$_2$ in the presence of a base, resulting in the formation of a [Cu^{II}-OOH)]$^+$ species (Equation C.9).[4-8] However, for Cu-tmpa and many other Cu pyridylalkylamine complexes, it has also been shown that these hydroperoxo species are often not stable over longer time periods.[6, 9] The appearance of the 405 nm band points to the formation of the hydroperoxo species, as the LMCT band of [Cu^{II}(tmpa)(OOH)]$^+$ has been reported at 379 nm or 410 nm (in acetone),[3] and at 379 nm (in MeCN).[4]

$$[Cu^{II}(tmpa)]^{2+} + HOO^- \rightarrow [Cu^{II}(tmpa)(OOH)]^+ \qquad (C.9)$$
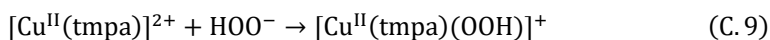
When H$_2$O$_2$ is added to a solution containing HNEt$_3^+$/NEt$_3$, the lowest energy d–d transition is blue-shifted by 55 nm to 805 nm. Additionally, a small band appears at 400 nm and a larger absorption peak appears at 305 nm. The resulting solution has a green colour, instead of the blue colour associated with [Cu^{II}(tmpa)(CH$_3$CN)]$^{2+}$. After 22 hours, the band around 400 nm has increased significantly, although hard to separate from the much larger peak at 300/305 nm. This again coincides with the decrease of absorption in the d–d band region, resulting in significant bleaching of the solution. The shoulder around 400 nm should be indicative of formation of [Cu^{II}(tmpa)(OOH)]$^+$. It is unlikely that the large peak at 300 nm is the hydroperoxo species, as this would be at least 80 nm blue-shifted compared to the lowest reported values. Neither does it correspond to the most likely decomposition product of the ligand, pyridine-2-carbaldehyde, which does not absorb above ~250 nm.[10]
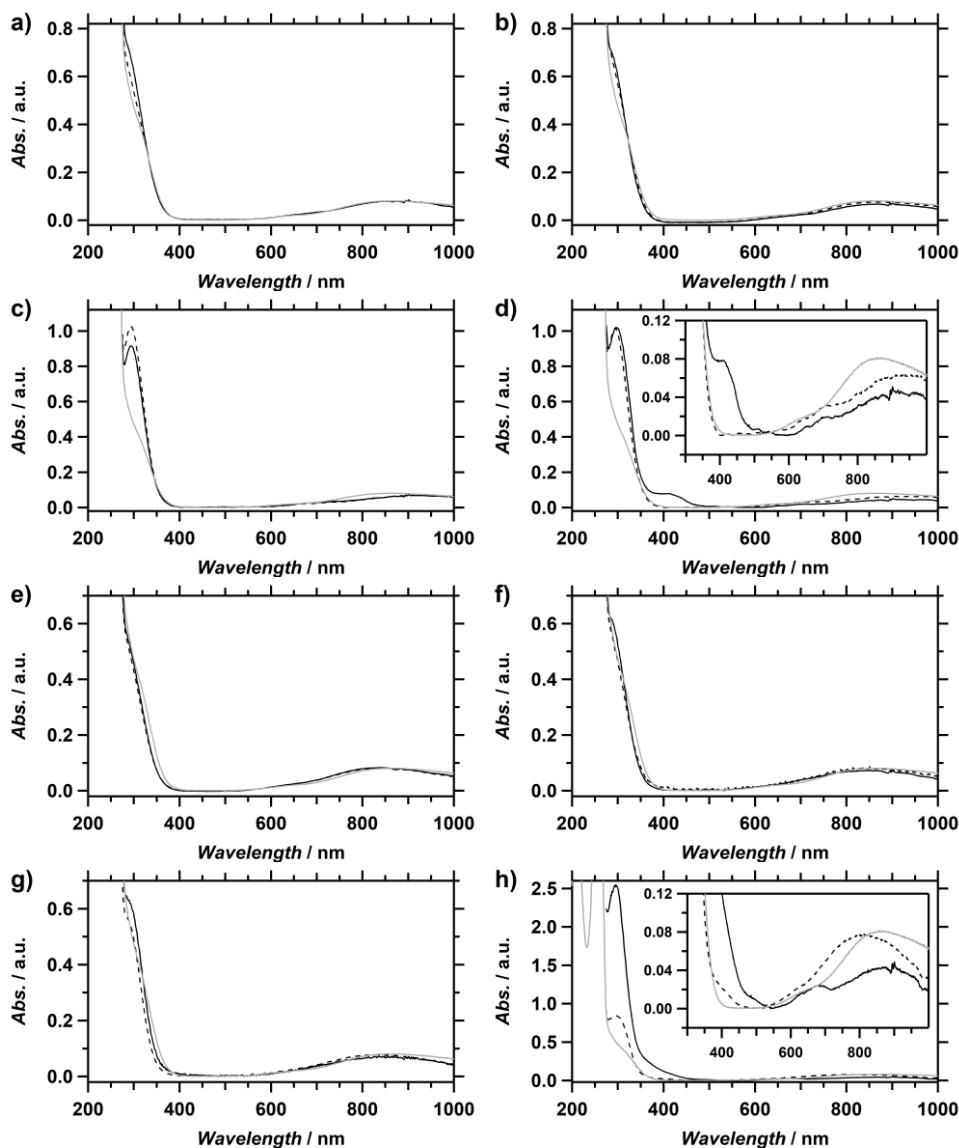
Figure C.12. UV-vis spectra of an electrolyte solution containing 0.30 mM Cu-tmpa and 0.10 M NBu_4PF_6 in MeCN under ambient atmosphere at room temperature (293 K), with several different acid or acid-conjugate base compositions. **a)** 100 mM HOAc, **b)** + 8.1 mM H_2O_2. **c)** 20 mM HOAc/OAcNBu$_4$, **d)** + 8.1 mM H_2O_2. **e)** 50 mM HNEt$_3$PF$_6$, **f)** + 8.1 mM H_2O_2. **g)** 50 mM HNEt$_3$PF$_6$/NEt$_3$, **h)** + 8.1 mM H_2O_2. Time after addition of Cu-tmpa to the electrolyte solution: 30 seconds (dashed line) or 22 hours (solid black line). Gray trace is the UV-vis absorbance in the absence of any acid or acid-conjugate base mixture, containing only the complex and supporting electrolyte. All UV-vis spectra were corrected for blank measurements of identical solutions in the absence of Cu-tmpa.

C.10   References

[1]   M. Yamada, K. D. Karlin, S. Fukuzumi, *Chemical Science* **2016**, *7*, 2856-2863.

[2]   J. Wang, M. P. Schopfer, S. C. Puiu, A. A. N. Sarjeant, K. D. Karlin, *Inorg. Chem.* **2010**, *49*, 1404-1419.

[3]   S. Kakuda, R. L. Peterson, K. Ohkubo, K. D. Karlin, S. Fukuzumi, *J. Am. Chem. Soc.* **2013**, *135*, 6513-6522.

[4]   A. Wada, M. Harata, K. Hasegawa, K. Jitsukawa, H. Masuda, M. Mukai, T. Kitagawa, H. Einaga, *Angew. Chem. Int. Ed.* **1998**, *37*, 798-799.

[5]   T. Fujii, A. Naito, S. Yamaguchi, A. Wada, Y. Funahashi, K. Jitsukawa, S. Nagatomo, T. Kitagawa, H. Masuda, *Chem. Commun.* **2003**, 2700-2701.

[6]   S. Yamaguchi, H. Masuda, *Science and Technology of Advanced Materials* **2005**, *6*, 34-47.

[7]   S. Kim, J. W. Ginsbach, J. Y. Lee, R. L. Peterson, J. J. Liu, M. A. Siegler, A. A. Sarjeant, E. I. Solomon, K. D. Karlin, *J. Am. Chem. Soc.* **2015**, *137*, 2867-2874.

[8]   A. Kunishita, J. D. Scanlon, H. Ishimaru, K. Honda, T. Ogura, M. Suzuki, C. J. Cramer, S. Itoh, *Inorg. Chem.* **2008**, *47*, 8222-8232.

[9]   Y. Syuhei, W. Akira, N. Shigenori, K. Teizo, J. Koichiro, M. Hideki, *Chem. Lett.* **2004**, *33*, 1556-1557.

[10]   E. P. Crowell, W. A. Powell, C. J. Varsel, *Anal. Chem.* **1963**, *35*, 184-189.

Appendix D

Supplementary Information for Chapter 5
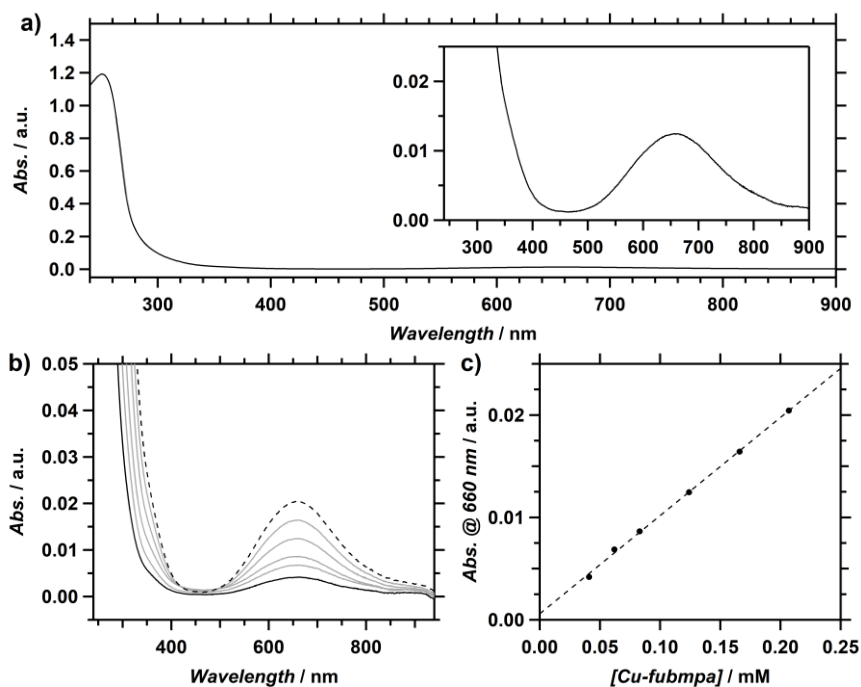
D.1 UV-vis spectra of Cu-fubmpa

Figure D.1. a) UV-vis spectrum of 0.12 mM Cu-fubmpa in water (MilliQ). The inset shows the Cu^{II} d-d transition. **b)** UV-vis spectra of 0.04 (solid black) to 0.2 (dashed) mM Cu-fubmpa in water (MilliQ). **c)** The linear relationship between catalyst concentration and the peak absorbance at 660 nm. Conditions: 293 K, 10 mm path length.

D.2 Cystallography data of Cu-fubmpa

Crystal data	
Chemical formula	$C_{19}H_{19}CuF_6N_3O_8S_2 \cdot H_2O$
M_r	677.05
Crystal system, space group	Monoclinic, $P2_1/c$
Temperature (K)	110
a, b, c (Å)	16.0028 (5), 9.8723 (3), 16.8915 (5)
β (°)	100.870 (3)
V (Å³)	2620.71 (14)
Z	4
Radiation type	Mo $K\alpha$
μ (mm⁻¹)	1.09
Crystal size (mm)	0.42 × 0.13 × 0.04

Data collection	
Diffractometer	SuperNova, Dual, Cu at zero, Atlas
Absorption correction	Gaussian *CrysAlis PRO* 1.171.39.29c (Rigaku Oxford Diffraction, 2017) Numerical absorption correction based on gaussian integration over a multifaceted crystal model. Empirical absorption correction using spherical harmonics, implemented in SCALE3 ABSPACK scaling algorithm.
T_{min}, T_{max}	0.463, 1.000
No. of measured, independent and observed [$I > 2\sigma(I)$] reflections	18658, 6012, 4878
R_{int}	0.032
$(\sin \theta/\lambda)_{max}$ (Å⁻¹)	0.650

Refinement	
$R[F^2 > 2\sigma(F^2)]$, $wR(F^2)$, S	0.035, 0.082, 1.04
No. of reflections	6012
No. of parameters	483
No. of restraints	501
H-atom treatment	H atoms treated by a mixture of independent and constrained refinement
$\Delta\rho_{max}$, $\Delta\rho_{min}$ (e Å⁻³)	0.42, -0.37

D.3   Selected bond distances and angles for Cu-fubmpa

Table D.1. Selected bond distances and bond angles of the crystal structure of Cu-fubmpa

Bond	Distance (Å)	Bond sequence	Angle (Å)	Bond sequence	Angle (Å)
Cu1–N1	1.975(2)	**N1–Cu1–N2**	83.65(7)	**N2–Cu1–O1W**	168.08(7)
Cu1–N2	2.037(2)	**N1–Cu1–N3**	166.31(8)	**N3–Cu1–O2**	90.89(7)
Cu1–N3	1.962(2)	**N1–Cu1–O1W**	98.01(8)	**N3–Cu1–O1W**	93.61(8)
Cu1–O1W	1.973(2)	**N1–Cu1–O2**	96.87(7)	**O2–Cu1–O1W**	87.14(7)
Cu1–O2	2.375(1)	**N2–Cu1–N3**	83.50(7)		
Cu1–O5	2.665(2)	**N2–Cu1–O2**	104.43(6)		

D.4   Diffusion Coefficients
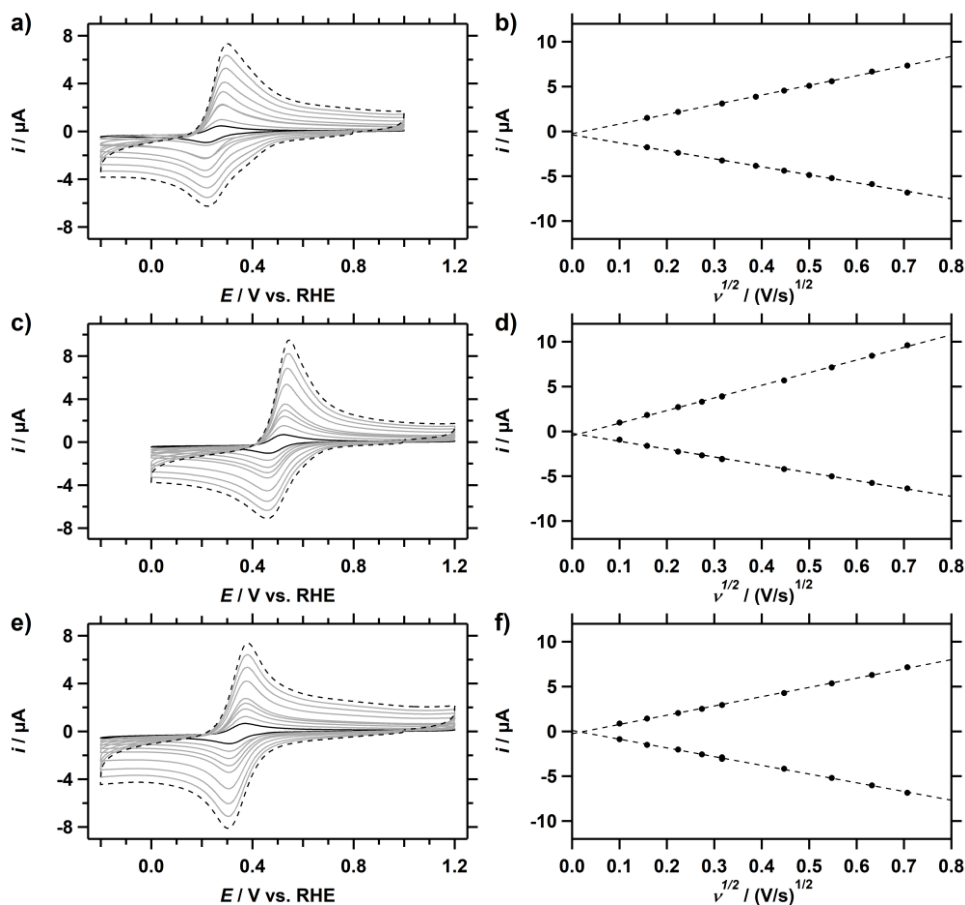
Figure D.2. CVs of Cu-fubmpa **(a)**, Cu-bpmpa **(b)**, and Cu-pmea **(c)** over a range of scan rates from 10 mV s^{-1} (solid black) to 500 mV s^{-1} (dashed). A concentration of 0.3 mM was used for each catalyst. Conditions: pH 7 PB ([PO$_4$] = 100 mM), 293 K, 0.0707 cm^2 electrode surface area.
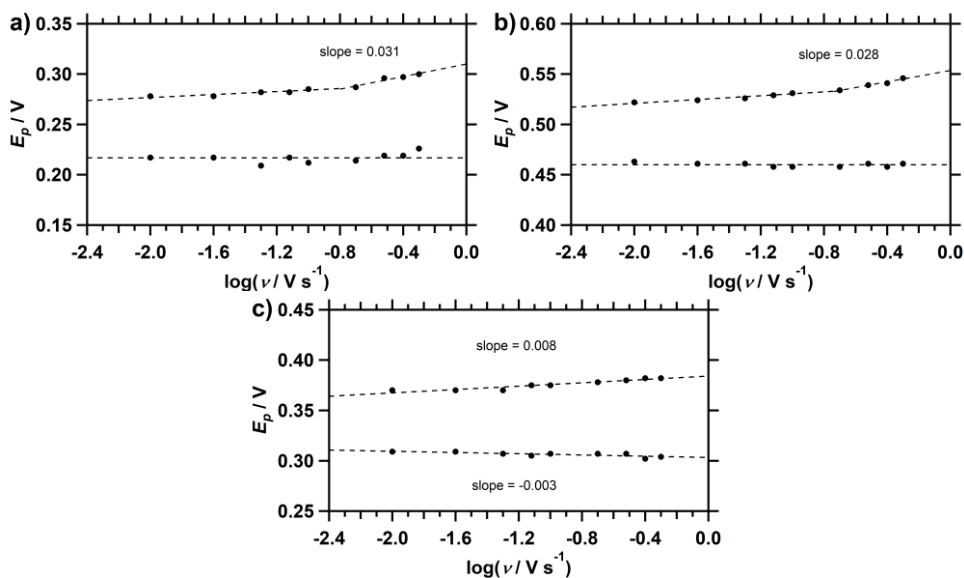
Figure D.3. Laviron plots showing the peak potentials as a function of the logarithm of the scan rate for Cu-fubmpa **(a)**, Cu-bpmpa **(b)**, and Cu-pmea **(c).** A concentration of 0.3 mM was used for each catalyst
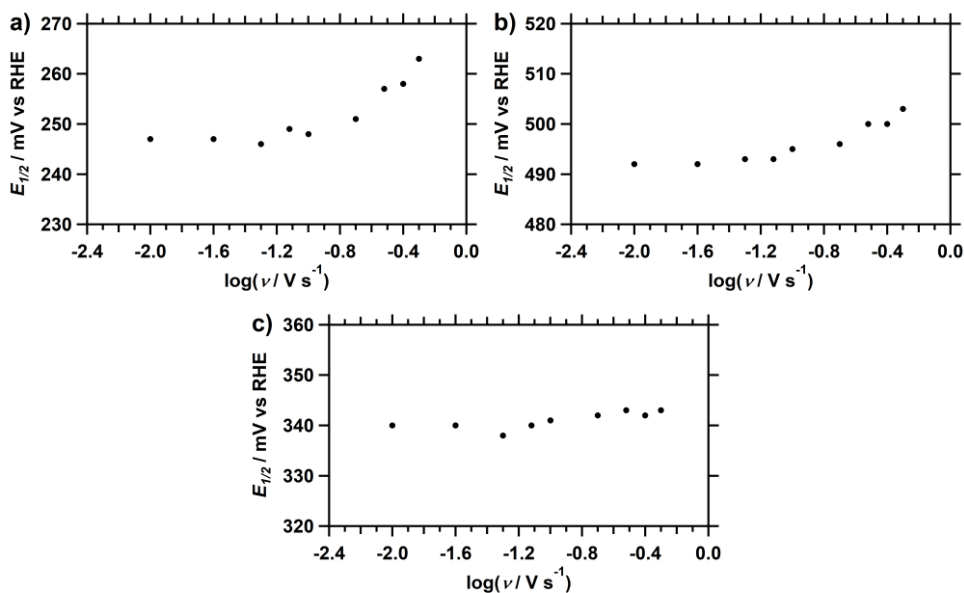

Figure D.4. Plot of redox half-wave potential as a function of scan rate for Cu-fubmpa **(a)**, Cu-bpmpa **(b)**, and Cu-pmea **(c).**
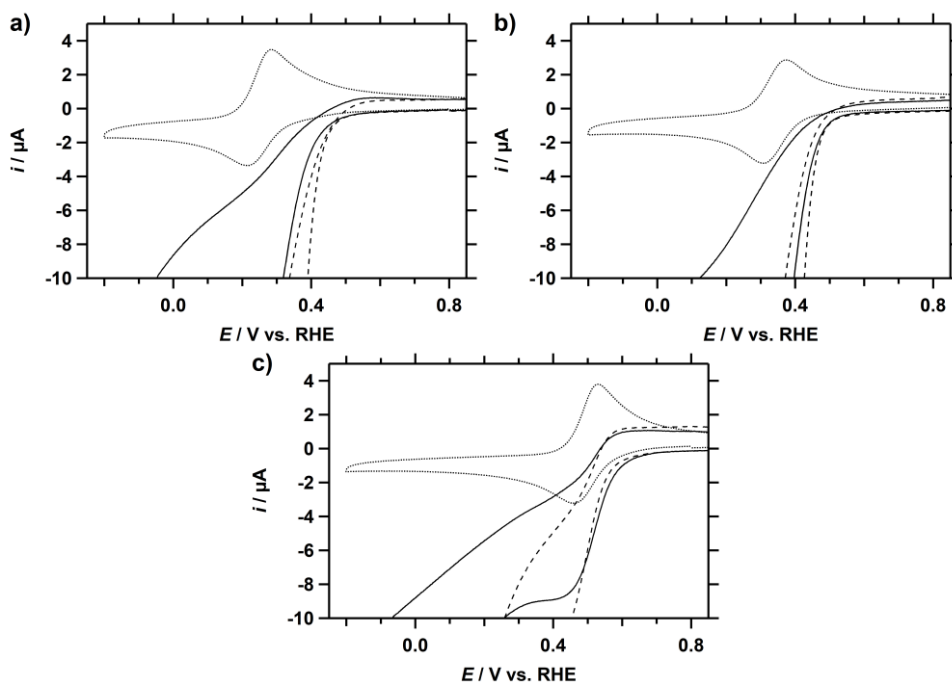
D.5 Comparison of onset ORR and HPRR.

Figure D.5. CVs of Cu-fubmpa **(a)**, Cu-pmea **(b)**, and Cu-bpmpa **(c)** in a PB pH 7 electrolyte solution under 1 atm Ar (dotted line), 1 atm O_2 (dashed line), or with 1.1 mM H_2O_2 under 1 atm Ar (solid line). For each catalyst, a concentration of 0.3 mM was used. Conditions: pH 7 PB ([PO_4] = 100 mM), 293 K, 100 mV s^{-1} scan rate, 0.0707 cm^2 electrode surface area.

D.6 Background corrected LSV of the ORR
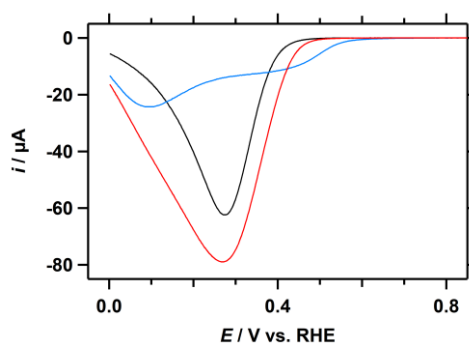
Figure D.6. LSV of Cu-fubmpa (black), Cu-pmea (red), and Cu-bpmpa (blue), under 1 atm O_2. A catalyst concentration of 0.3 mM was used for each complex. Conditions: pH 7 PB ([PO_4] = 100 mM), 293 K, 100 mV s^{-1} scan rate, 0.0707 cm^2 electrode surface area.

D.7 Catalytic ORR activity at low catalyst concentrations
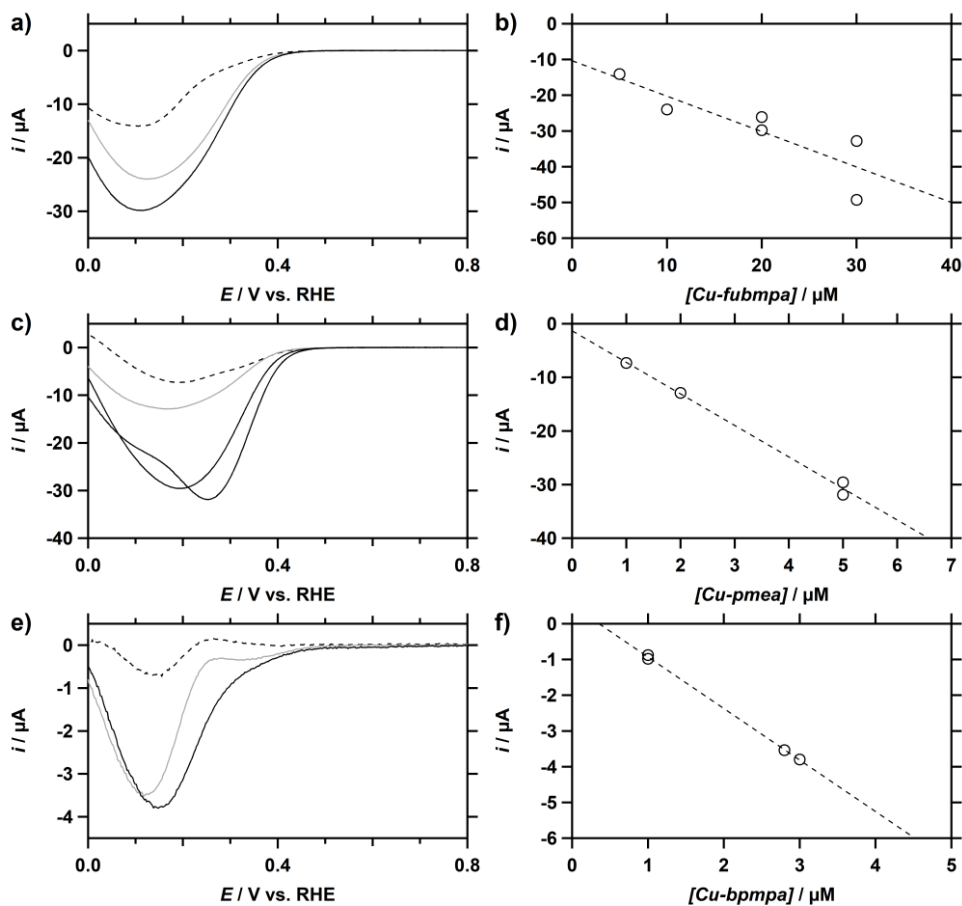

Figure D.7. Background-corrected LSV of-fubmpa **(a)**, Cu-pmea **(c)**, and Cu-bpmpa **(e)** at different catalyst concentrations in the presence of 1 atm O_2. On the right, the corresponding peak catalytic current obtained from the LSV of Cu-fubmpa **(b)**, Cu-pmea **(d)**, and Cu-bpmpa **(f)** as a function of catalyst concentration. Conditions: pH 7 PB ([PO_4] = 100 mM), 293 K, 100 mV s^{-1} scan rate, 0.0707 cm^2 electrode surface area.

D.8 DPV of Cu-pmea in the presence of dioxygen
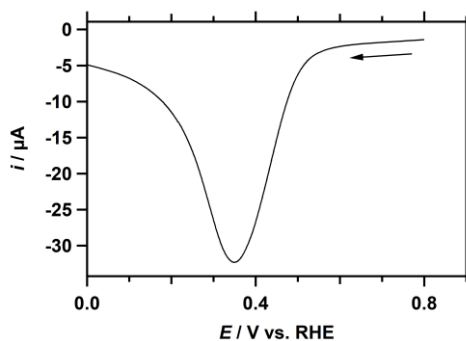
Figure D.8. DPV of Cu-pmea (0.3 mM) in the presence of 1 atm. O_2. Conditions: pH 7 PB ([PO_4] = 100 mM), 293 K, 100 mV s^{-1} scan rate, 0.0707 cm^2 electrode surface area.
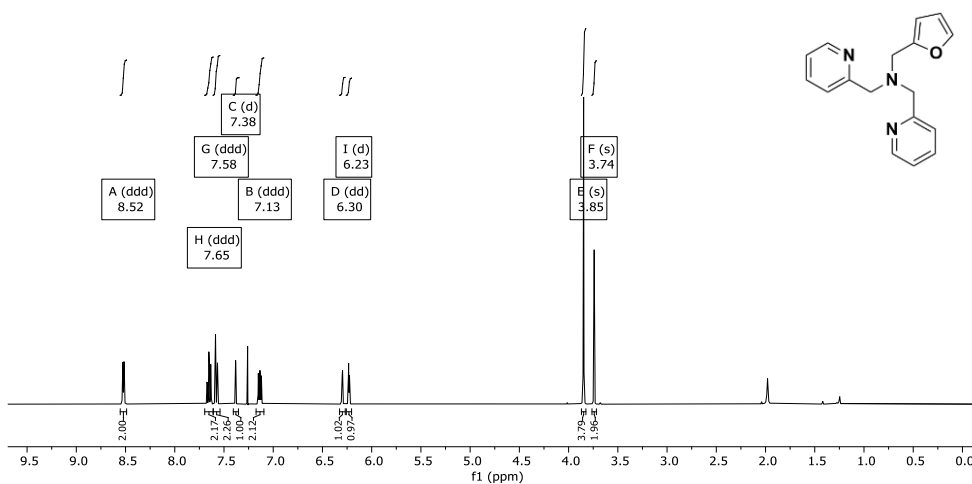
D.9 NMR spectra

Figure D.9. ^{1}H NMR spectrum of *N*-(Furan-2-ylmethyl)-*N*-[bis(2-pyridyl)methyl]amine (fubmpa) in CDCl$_3$.
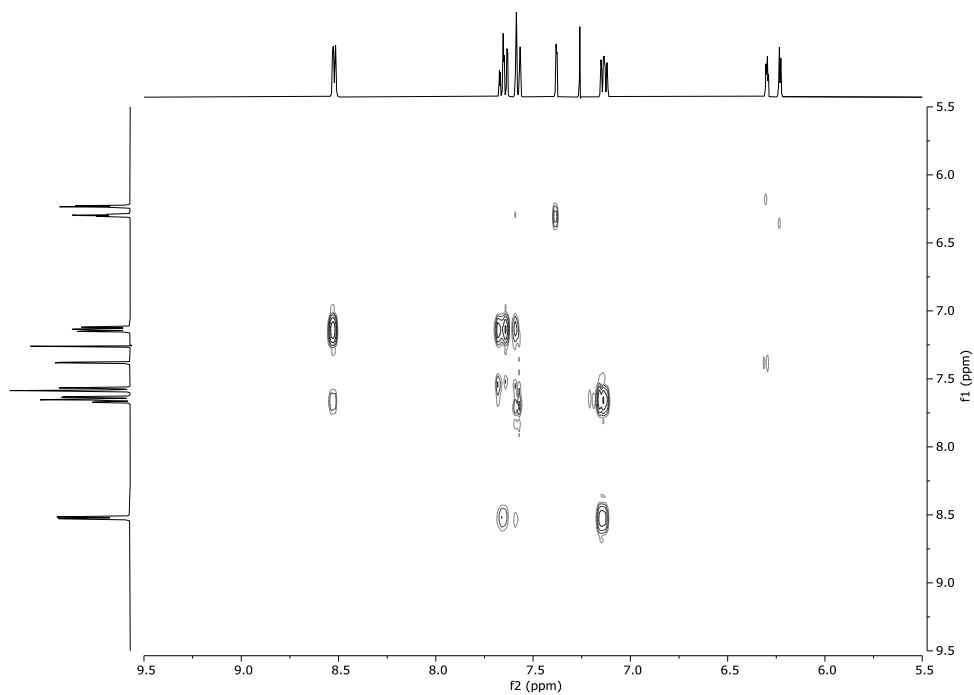
Figure D.10. ^{1}H-^{1}H COSY NMR spectrum of *N*-(Furan-2-ylmethyl)-*N*-[bis(2-pyridyl)methyl]amine (fubmpa) in CDCl$_3$.
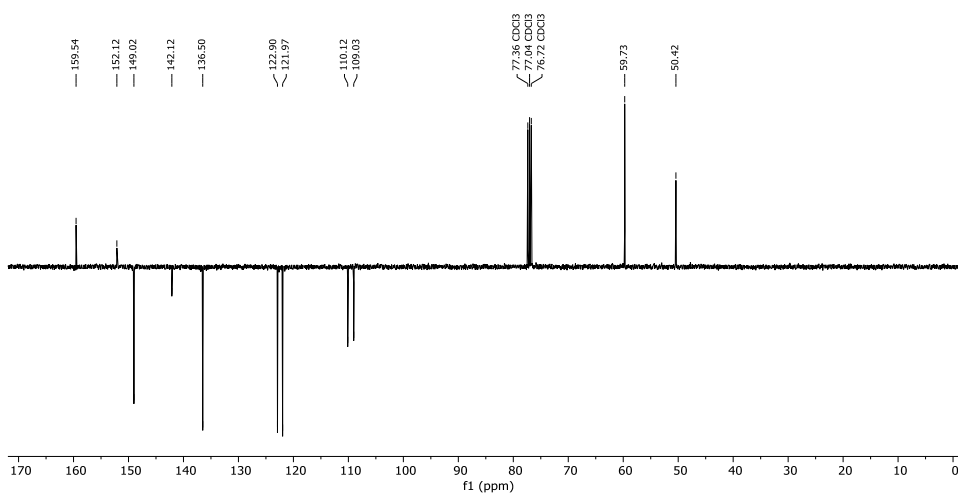

Figure D.11. ^{13}C NMR spectrum of *N*-(Furan-2-ylmethyl)-*N*-[bis(2-pyridyl)methyl]amine (fubmpa) in CDCl$_3$.
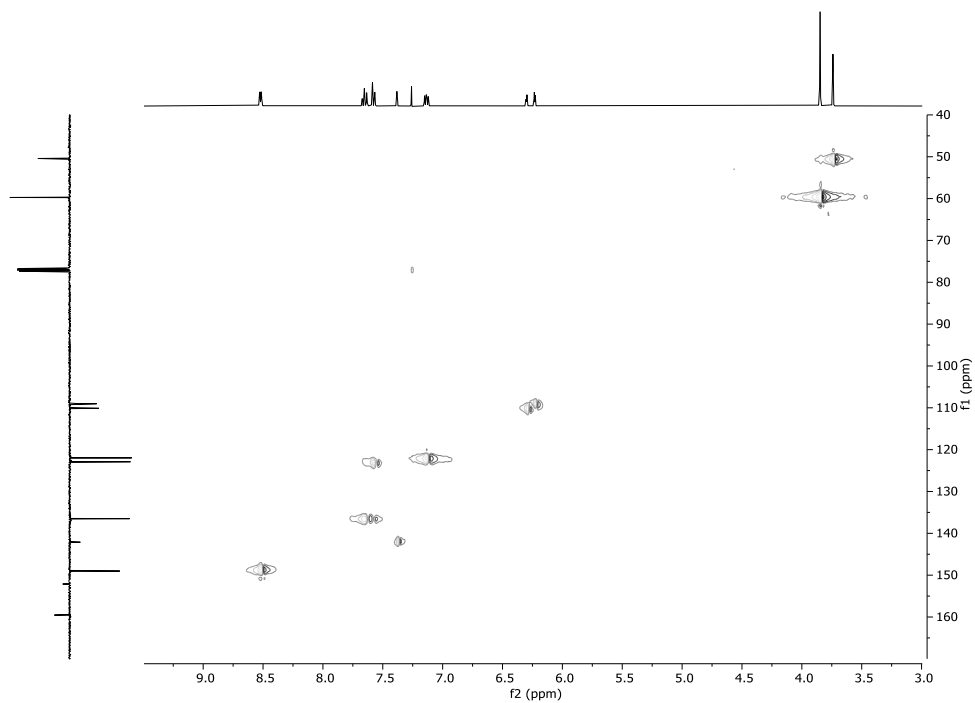
Figure D.12. 2D HSQC spectrum of *N*-(Furan-2-ylmethyl)-*N*-[bis(2-pyridyl)methyl]amine (fubmpa) in CDCl₃.
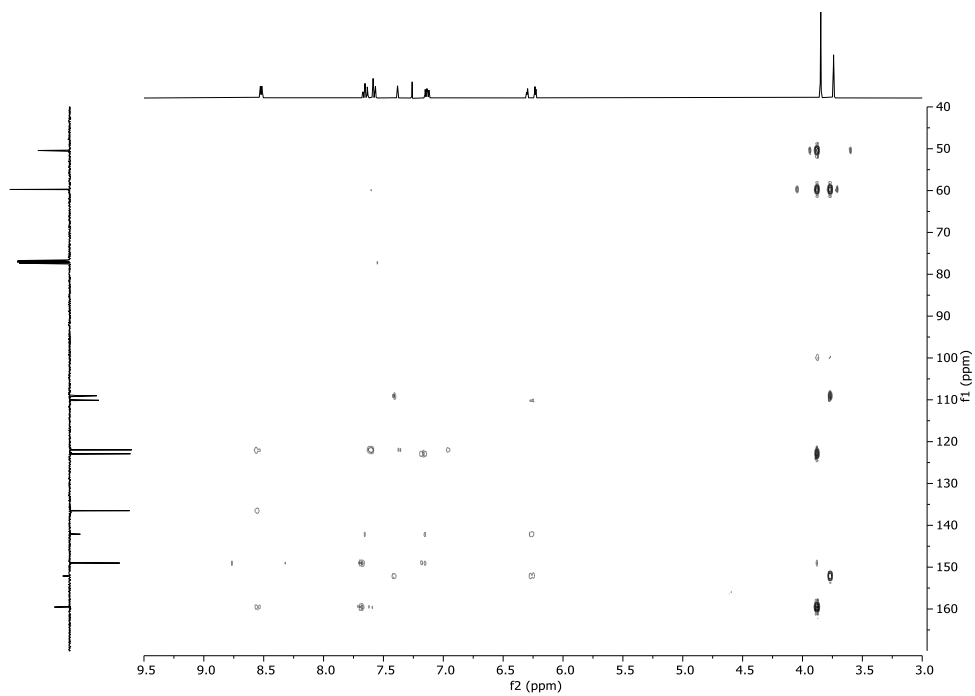
Figure D.11. 2D HMBC spectrum of *N*-(Furan-2-ylmethyl)-*N*-[bis(2-pyridyl)methyl]amine (fubmpa) in CDCl₃.